J. Space Weather Space Clim. 2018, 8, A04

https://doi.org/10.1051/swsc/2017031

SWSC

Available online at:
www.swsc-journal.org

Measurement, Specification and Forecasting of the Solar Energetic Particle Environment and GLEs

RESEARCH ARTICLE OPEN ACCESS

Two solar proton fluence models based on ground level enhancement observations

Osku Raukunen[1,*], Rami Vainio[1], Allan J. Tylka[2], William F. Dietrich[3], Piers Jiggens[4], Daniel Heynderickx[5], Mark Dierckxsens[6], Norma Crosby[6], Urs Ganse[7] and Robert Siipola[1]

[1] Department of Physics and Astronomy, University of Turku, 20014 Turku, Finland
[2] Emeritus, NASA Goddard Spaceflight Center, Greenbelt, 20771 MD, USA
[3] Consultant, Prospect Heights, 60070 IL, USA
[4] ESA Space Environments & Effects section (TEC-EES), ESA-ESTEC, Keplerlaan 1, 2201 AZ Noordwijk, Netherlands
[5] DH Consultancy, Leuven, Belgium
[6] Royal Belgian Institute for Space Aeronomy, Avenue Circulaire 3, 1180 Uccle, Belgium
[7] Department of Physics, University of Helsinki, Helsinki, Finland

Received 7 July 2017 / Accepted 10 November 2017

Abstract – Solar energetic particles (SEPs) constitute an important component of the radiation environment in interplanetary space. Accurate modeling of SEP events is crucial for the mitigation of radiation hazards in spacecraft design. In this study we present two new statistical models of high energy solar proton fluences based on ground level enhancement (GLE) observations during solar cycles 19–24. As the basis of our modeling, we utilize a four parameter double power law function (known as the Band function) fits to integral GLE fluence spectra in rigidity. In the first model, the integral and differential fluences for protons with energies between 10 MeV and 1 GeV are calculated using the fits, and the distributions of the fluences at certain energies are modeled with an exponentially cut-off power law function. In the second model, we use a more advanced methodology: by investigating the distributions and relationships of the spectral fit parameters we find that they can be modeled as two independent and two dependent variables. Therefore, instead of modeling the fluences separately at different energies, we can model the shape of the fluence spectrum. We present examples of modeling results and show that the two methodologies agree well except for a short mission duration (1 year) at low confidence level. We also show that there is a reasonable agreement between our models and three well-known solar proton models (JPL, ESP and SEPEM), despite the differences in both the modeling methodologies and the data used to construct the models.

Keywords: Sun / energetic particle / ground level enhancement (GLE) / modelling / space weather

1 Introduction

In some of the most extreme solar energetic particle (SEP) events, particles can be accelerated up to GeV energies. These energies are sufficient for particles to reach the atmosphere of the Earth, where their interactions produce showers of secondary particles all the way to the ground level; hence, these events are known as ground level enhancements (GLEs). These secondary particles can be detected with neutron monitors (NMs; Simpson et al., 1953; Simpson, 1958) on ground as increases in intensity above the background produced by the galactic cosmic rays (GCRs). Since 1942, 72 GLEs have been observed (Cliver et al., 1982; Cliver, 2006; Gopalswamy et al., 2013). The latest GLE occurred on September 10, 2017, and, at the time of writing, no analysis of the event exists in the literature. In addition, an SEP event of January 6, 2014, led to a small counting-rate increase in two NMs at the South Pole (Thakur et al., 2014), but this event does not meet the criteria of detection in at least two different locations, and is therefore not included in the official GLE database maintained by the University of Oulu.[1] It should be taken into account that before the construction of the worldwide neutron monitor network during the International Geophysical Year (IGY; between July 1957 and December 1958) the observation of smaller GLEs was not completely reliable (Shea and Smart, 2000). The occurrence rate of GLEs varies both with solar

*Corresponding author: oajrau@utu.fi

[1] http://gle.oulu.

Table 1. Observed GLEs since 1942 and their solar event associations. Data references are given in the notes below the table.

GLE	Episode	Solar cycle	Date	Flare onset[a]	Flare max[a]	Solar coordinate[b]	Active region[c]	GLE onset[d]
1		17	1942-02-28	1200[e]	1205[e]	N07E04	1182, 12	1200
2		17	1942-03-07	0442[e]	0450[e]	N07W90	N.R.	0500
3		18	1946-07-25	1615	1640	N22E15	1242, 51	1645
4		18	1949-11-19	1029	1033	S02W70	1286, 23	1044
5	1	19	1956-02-23	0331	0342	N23W80	3400	0343
6	2	19	1956-08-31	1226	1243	N15E15	3646	1250
7	3	19	1959-07-16	2114	2132	N16W31	5265	2500
8	4	19	1960-05-04	1000	1016	N13W90	5642	1030
9	5	19	1960-09-03	0037	0108	N18E88	5837	0200
10	6	19	1960-11-12	1315	1330	N27W04	5925	1335
11	6	19	1960-11-15	0207	0221	N25W35	5925	0230
12	6	19	1960-11-20	2017	2020	N25W113	5925	2058
13	7	19	1961-07-18	0920	1005	S07W59	6171	1015
14	7	19	1961-07-20	1553	N.R.	S06W90	6171	1615
15	8	20	1966-07-07	0025	0040	N35W48	8362	0055
16	9	20	1967-01-28	0206[f]	N.R.	N22W154	8687[g]	0302
17	9	20	1967-01-28	0714[f]	N.R.	N22W154	8687[g]	0810
18	10	20	1968-09-29	1618	1623	N17W51	9678	1710
19	11	20	1968-11-18	1017	1035	N21W87	9760	1038
20	12	20	1969-02-25	0900	0913	N13W37	9946	0915
21	13	20	1969-03-30	0304[f]	N.R.	N19W106	9994	0400
22	14	20	1971-01-24	2309	2330	N19W49	11128	2328
23	15	20	1971-09-01	1904[f]	N.R.	S11W120	N.R.	2000
24	16	20	1972-08-04	0621	0635	N14E08	11976	1330
25	16	20	1972-08-07	1505	1528	N14W37	11976	1528
26	17	20	1973-04-29	2056	2108	N13W73	12322	2143
27	18	21	1976-04-30	2048	2103	S08W46	700	2123
28	19	21	1977-09-19	0955	1042	N08W57	899	1100
29	19	21	1977-09-24	0512[f]	N.R.	N10W120	899	0608
30	20	21	1977-11-22	0945	1007	N24W40	939	1013
31	21	21	1978-05-07	0327	0336	N23W72	1095	0336
32	22	21	1978-09-23	0944	1010	N35W50	1294	1028
33	23	21	1979-08-21	0611	0613	N17W40	1926	0640
34	24	21	1981-04-10	1632	1703	N07W36	3025	1745
35	25	21	1981-05-10	0712	0731	N03W75	3079	0615
36	26	21	1981-10-12	0622	0636	S18E31	3390	0650[h]
37	27	21	1982-11-26	0230	0237	S12W87	3994	0300
38	28	21	1982-12-07	2336[i]	2354[i]	S19W86	4007	2350
39	29	21	1984-02-16	0815[j]	0900[k]	W130	4408	0905
40	30	22	1989-07-25	0839	0843	N26W85	5603	0850
41	31	22	1989-08-16	0108	0117	S15W85	5629	0145
42	32	22	1989-09-29	1047	1133	W100	5698	1135
43	32	22	1989-10-19	1229	1245	S25E09	5747	1310
44	32	22	1989-10-22	1708	1757	S27W32	5747	1810
45	32	22	1989-10-24	1736	1831	S29W57	5747	1820
46	33	22	1989-11-15	0638	0705	N11W28	5786	0705
47	34	22	1990-05-21	2212	2217	N34W37	6063	2230
48	34	22	1990-05-24	2046	2049	N36W76	6063	2110
49	34	22	1990-05-26	2045	2058	W100	6063	2055
50	34	22	1990-05-28	0428[i]	0433[i]	W120	6063	1000
51	35	22	1991-06-11	0209	0229	N32W15	6659	0230
52	35	22	1991-06-15	0633[i]	0831[i]	N36W70	6659	0840
53	36	22	1992-06-25	1947	2011	N10W68	7205	2035
54	37	22	1992-11-02	0231	0308	W100	7321	0350
55	38	23	1997-11-06	1149	1155	S18W63	8100	1210
56	39	23	1998-05-02	1331	1342	S15W15	8210	1355
57	39	23	1998-05-06	0758	0809	S15W64	8210	0825

Table 1. (continued).

GLE	Episode	Solar cycle	Date	Flare onset[a]	Flare max[a]	Solar coordinate[b]	Active region[c]	GLE onset[d]
58	40	23	1998-08-24	2150	2212	N35E09	8307	2250
59	41	23	2000-07-14	1003	1024	N22W07	9077	1030
60	42	23	2001-04-15	1319	1350	S20W84	9415	1400
61	42	23	2001-04-18	0211	0214	W115	9415	0235
62	43	23	2001-11-04	1603	1620	N07W19	9684	1700
63	44	23	2001-12-26	0432	0540	N08W54	9742	0530
64	45	23	2002-08-24	0049	0112	S02W81	10069	0120
65	46	23	2003-10-28	0951	1110	S16E08	10486	1120
66	46	23	2003-10-29	2037	2049	S15W02	10486	2105
67	46	23	2003-11-02	1703	1725	S14W56	10486	1730
68	47	23	2005-01-17	0938[l]	0952[l]	N13W23	10720	0955
69	47	23	2005-01-20	0636	0701	N12W58	10720	0650
70	48	23	2006-12-13	0214	0240	S06W23	10930	0245
71	49	24	2012-05-17	0125	0147	N11W76	11476	0143

Notes. [a]GLE1-32: Hα onset and maximum from Cliver et al. (1982); GLE33-69: X-ray onset and maximum from Belov et al. (2010); GLE70: X-ray onset and maximum from NOAA STP X-ray database; GLE71: X-ray onset and maximum from Gopalswamy et al. (2013). [b]GLE1-32: Cliver et al. (1982); GLE33-69: Cliver (2006); GLE70: NOAA STP X-ray database; GLE71: Gopalswamy et al. (2013). [c]GLE1-4: Meudon rot/n from the Quarterly Bulletin on Solar Activity; GLE5-21: McMath plage region from Švestka and Simon (1975); GLE22-26: McMath plage region from NOAA STP Hα database; GLE27-69: NOAA AR from Belov et al. (2010); GLE70: NOAA AR from NOAA STP X-ray database; GLE71: NOAA AR from Gopalswamy et al. (2013). [d]GLE1-32: Cliver et al. (1982); GLE33-53: Firoz et al. (2010); GLE54: Shea et al. (1995); GLE55-70: Gopalswamy et al. (2012); GLE71: Gopalswamy et al. (2013). [e]Hα flash phase onset and maximum. [f]GLE onset time minus the average time difference between the flare onset and GLE onset of GLEs 1–32. [g]Dodson and Hedeman (1969). [h]Kudela et al. (1993). [i]NOAA STP X-ray database. [j]GLE onset time minus the average time difference between the flare onset and GLE onset of GLEs 33–54. [k]Cliver (2006). [l]Gopalswamy et al. (2012).

activity and from cycle to cycle; the most dramatic change in GLE activity has been the decrease from 16 GLEs during solar cycle 23 to only one during the ongoing cycle 24 (between December 2008 and March 2017). A detailed list of GLEs 1–71 and their solar event associations is presented in Table 1. We note that since GLE 72 occurred after the release of our model 1 (see Sect. 5), it is not included in the analysis presented in this paper.

According to the two-class paradigm (e.g., Reames, 1999; Reames, 2013, and references therein), SEP events are categorized as impulsive events relating to particle acceleration in solar flares, or gradual events, associated with shocks driven by coronal mass ejections (CMEs). Impulsive events generally have shorter durations, smaller particle fluences and more compact spatial scales when compared to gradual events. Another distinguishing factor is the particle composition: impulsive events are characterized as electron- and ^{3}He-rich and with enhanced abundances of heavy ions (e.g., Reames et al., 1985; Reames, 1988), whereas the particle composition of gradual events more or less resembles that of the solar corona (e.g., Meyer, 1985). Although GLEs are usually considered as extreme examples of gradual events, some studies suggest that GLEs have a direct flare component, based on their temporal behaviour (Grechnev et al., 2008; McCracken et al., 2008), or particle composition and charge states (Cohen et al., 1999; Mason et al., 1999; Möbius et al., 1999). It has also been suggested that the energy-dependent composition and charge states in these events can be understood in terms of evolving shock-normal angle in a shock acting on remnant flare suprathermals from earlier flare activity (Tylka et al., 2005; Tylka and Lee, 2006; Sandroos and Vainio, 2007; Sandroos and Vainio, 2009).

SEP events can be considered as one of the most important features of space weather (e.g., Vainio et al., 2009). As the most energetic class of SEP events, GLEs are important drivers of space weather phenomena. For spacecraft outside the Earth's trapped radiation belts and the shelter provided by the Earth's magnetic field, SEPs constitute the most severe radiation hazard. Radiation effects caused by SEPs include degradation of electronic components and solar cells and single event effects (SEE) including latchups and upsets (e.g., Feynman and Gabriel, 1996). In addition to being harmful to electronics, ionizing particle radiation is dangerous to biological organisms. Astronauts on space missions and even aircraft crews and passengers on high altitude polar flights are susceptible to radiation hazards. Effects of radiation on humans are divided into two categories: early (deterministic) effects, caused by sudden exposure to a large dose of radiation, which include nausea or even death, and late (stochastic) effects, usually manifesting as different forms of cancer. Effects of space weather on both electronic and biological systems have been reviewed in e.g., Facius and Reitz (2007); Lanzerotti (2007); Vainio et al. (2009); Singh et al. (2010), and references therein.

In order to mitigate the effects of SEPs in spacecraft design in reliable and cost-effective ways, the SEP environment must be accurately modeled. Given the probabilistic nature of SEP event occurrence, the modeling approach needs to be statistical. There is a major need for models of high energy protons in heavily shielded environments such as human spaceflight or orbits well within the magnetosphere, where the high energy part of the spectrum becomes dominant. The purpose of this study is to present two new high energy solar

proton models based on long-term observations of high energy SEP events. We start by giving a short overview of advances in the modeling of solar energetic particles (Sect. 2), then describe the energy spectra of GLEs (Sect. 3) and analyze their timing (Sect. 4). In Section 5 and Section 6 we present details of our two models, compare the models in Section 7 and present a summary and discussion in Section 8.

2 Previous models of SEPs

The first widely accepted probabilistic solar proton fluence model was presented by King, (1974). His model was based on observations of >10 to >100 MeV protons during the solar cycle 20. The fluence for that cycle was dominated by the GLEs of August 1972, which King, (1974) considered "anomalously large", in contrast to "ordinary" events. The model assumed that the spectrum of all predicted anomalously large events would resemble that of August 1972, and that the fluences of the ordinary events follow log-normal distribution.

An update for the King model, known as the Jet Propulsion Laboratory (JPL) model, was developed by Feynman et al., (1990, 1993). Using data from solar cycles 19–21, they showed that the distribution of event sizes during the active part of the solar cycle can be modeled with a continuous log-normal distribution, thus removing the need to divide events into ordinary and anomalously large. The JPL model uses Monte Carlo simulations to calculate the total fluence accumulated during a mission at a certain confidence level.

The JPL model was in turn improved by Rosenqvist et al., (2005), who studied the effect of the fitting procedure, fluence thresholds and the inclusion of different data sources on the model. They used >10 MeV proton data from January 1974 to May 2002 and provided to the public all the data and tools needed to update the model. Their work was further developed by Glover et al., (2008), who extended the study to >30 MeV protons.

Another solar proton fluence model is the Emission of Solar Protons (ESP) model (Xapsos et al., 2000), which predicts integral fluences at energies from >1 MeV to >300 MeV during the active part of the solar cycle. It applies a lognormal fit to the observed yearly fluences which is then extrapolated to longer mission durations. Xapsos et al. (2004) developed the model further into the Prediction of Solar particle Yields for Characterization of Integrated Circuits (PSYCHIC) model, which predicts proton spectra up to >327 MeV and considers solar minimum and maximum periods. The PSYCHIC model was extended to also predict cumulative solar heavy ion fluences (Xapsos et al., 2007). In addition, a model for solar electrons has been developed based on the approach of the ESP model (Taylor et al., 2011).

Another approach to solar proton modeling is the Solar Energetic Particle Environment Modelling (SEPEM) (Jiggens et al., 2012), which is based on "virtual timelines" rather than traditional Monte Carlo approaches which base the number of SEP events to be sampled from an event frequency distribution. Finally, in the Moscow State University (MSU) model by Nymmik (1998); Nymmik (1999), the occurrence rate of the particle events follows the solar activity level, parameterised by the Wolf sunspot number. Another property of the MSU model that differentiates it from other models is that the shape of the fluence spectra of generated events is modeled instead of the fluence distribution being derived in each individual energy channel. More recently Atwell et al. (2016) have provided a probabilistic model of SEP fluences and doses during periods of low solar activity, with monthly smoothed sunspot number less than 50. More extensive space particle radiation model reviews and comparisons can be found for example in Vainio et al. (2009); Jiggens et al. (2012); Xapsos et al. (2013).

3 Integral fluence spectra of GLEs

Tylka and Dietrich (2009) developed a method for analysing data from the worldwide neutron monitor network. They derived normalized, event-integrated proton spectra for 53 of the 66 GLE events occurring between 1956–2009. Their results agreed well with the fluences measured by IMP-8 (McGuire et al., 1986), SAMPEX (Baker et al., 1993) and GOES (Onsager et al., 1996) spacecraft at energies of ~300–700 MeV, corresponding to rigidities of ~0.81–1.43 GV. Furthermore, they showed that the integral fluence spectra in rigidity from combined spacecraft and neutron monitor measurements can be represented with a double power law function, also known as the Band function (Band et al., 1993):

$$J(>R) = \begin{cases} J_0 \left(\frac{R}{1\mathrm{GV}}\right)^{-\gamma_1} \exp\left(-\frac{R}{R_0}\right), & R < (\gamma_2-\gamma_1)R_0 \equiv R_1 \\ J_0 \left(\frac{R_1}{1\mathrm{GV}}\right)^{-\gamma_1} \exp\left(-\frac{R_1}{R_0}\right)\left(\frac{R}{R_1}\right)^{-\gamma_2}, & R \geq R_1 \end{cases} \quad (1)$$

Here $J(>R)$ is the omnidirectional event-integrated integral fluence in units of cm^{-2}, J_0 is an overall fluence normalization coefficient, γ_1 is the low rigidity power law index, γ_2 the high rigidity power law index and $(\gamma_2-\gamma_1)R_0 \equiv R_1$ is the breakpoint rigidity. The Band function is constructed in such a way that both the function and its first derivative are continuous. Recently, the Band function has been shown to approximate well the energetic particle spectra in the GLEs of solar cycle 23 measured by instruments on the ACE, GOES, SAMPEX and STEREO spacecraft (Mewaldt et al., 2012) and GLE71 measured by the PAMELA experiment (Asvestari et al., 2017), as well as proton and heavy ion spectra of large SEP events measured by instruments on the ACE, SAMPEX, SOHO and GOES spacecraft (Desai et al., 2016a, b). The original Tylka and Dietrich (2009) GLE analysis was extended through 2012 using data from GOES spacecraft[2] and the worldwide NM network. The analysis uses timelines of pressure-corrected neutron monitor counts obtained primarily from online public archives at the US National Geophysical Data Center (NGDC)[3] and the Bartol Research Institute[4], as well as a few other public station-websites and online archives, some of

[2] http://satdat.ngdc.noaa.gov/sem/goes/

[3] http://www.ngdc.noaa.gov/stp/space-weather/interplanetary-data/cosmic-rays/cawses-database/

[4] http://neutronm.bartol.udel.edu

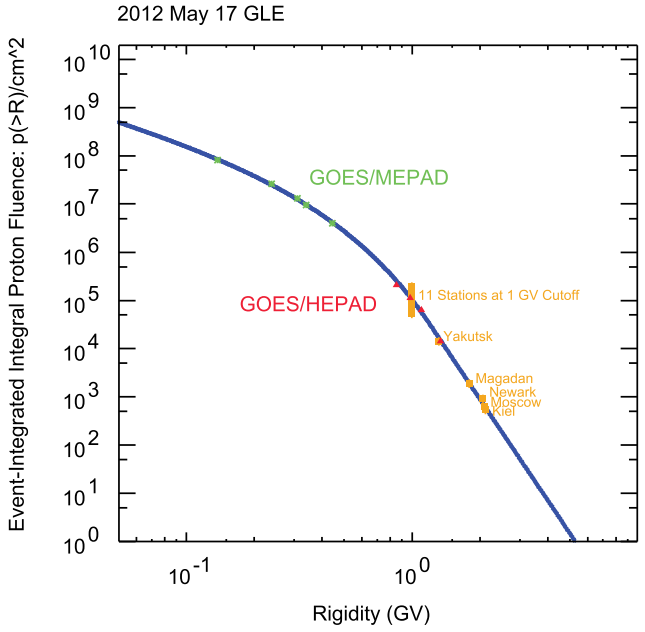

Fig. 1. Event-integrated proton fluence spectrum for GLE 71. NM observations are shown in orange, GOES/MEPAD in green, GOES/HEPAD in red and the Band-fit spectrum in blue.

which are no longer available. The analysis starts with defining the uncorrected integral solar proton fluence as the product of the integral GCR fluence (Nymmik et al., 1992; Smart et al., 2006), which depends on the cutoff rigidity of the neutron monitor, R_i, and time, T, and the fractional increase in the NM counts, i.e.,

$$\tilde{F}_{SEP,i}(>R_i) = F_{GCR}(>R_i, T)\cdot\left(\frac{\Delta N_{GLE,i}}{N_{GCR,i}}\right) \quad (2)$$

The uncorrected fluence is then corrected with a factor $C(R_i, T, \gamma)$, which also depends on the cutoff rigidity and time, as well as the spectral shape of the solar protons, which is assumed to be a power law in rigidity. The correction factor can be evaluated numerically as

$$C(R_i, T, \gamma) = \frac{\int_{R_i}^{\infty} s(r)\mathrm{d}r}{\int_{R_i}^{\infty} g(r,T)\mathrm{d}r}\cdot\frac{\int_{R_i}^{\infty} y(r)g(r,T)\mathrm{d}r}{\int_{R_i}^{\infty} y(r)s(r)\mathrm{d}r}, \quad (3)$$

where $s(r)$ is the differential solar proton spectrum, $g(r)$ is the differential GCR spectrum, and $y(r)$ is the NM yield function (Clem and Dorman, 2000). The correction factor and the corrected fluence for each NM i is then calculated for a range of power law indices γ. For each GLE, a least-squares fit to a power law in rigidity is performed on the corrected fluences, and the value of γ that gives the best fit is selected. As an example of the corrected NM fluences, the integral proton spectrum of GLE 71 is shown in Figure 1. The NM observations are shown in orange, GOES observations in green (MEPAD) and red (HEPAD), and the Band-fit spectrum in blue.

For the analysis of the fluence spectra of GLEs we utilize a dataset with spectral parameters for 59 GLEs occurring in 1956–2012. During the years, 67 GLEs occurred in total, but eight of them had too small fluences for the Band-fits to be reliable. The smaller events also need to be taken into account when modeling the proton fluences; this will be discussed in more detail in both of our model descriptions. The spectral parameters and their uncertainties are given in Table 2. Figure 2 shows the event-integrated fluences above 1 GV for all 59 GLEs. The fluences and their uncertainties were calculated as the geometric means and geometric standard deviations of large samples ($N = 10^5$) of fluence values generated for each event by sampling each Band-fit parameter from normal distributions centered on their best-fit values with standard deviations given by their error estimates. Note that here and later in the paper we plot fluences in units of $\mathrm{cm}^{-2}\,\mathrm{sr}^{-1}$, i.e., the omnidirectional fluences divided by 4π.

Five events (GLE43, GLE58, GLE59, GLE62 and GLE65) were analysed separately for their GLE and energetic storm particle (ESP[5]) components. In addition, GLE42 was analysed separately for the first 75 minutes and the following 61 hours. The GLE components of these events are marked with additional red squares and the ESP components are shown in red in Figure 2 (which also shows the monthly sunspot number[6] as an overall measure of solar activity). Three of the GLE components (GLEs 58, 59 and 65) have higher fluences at R>1 GV than their separately analysed counterparts, and the reverse is true for the other three. Neither of the separately analysed components seem to have noticeably different fluence distributions compared to the other datapoints. In both of our model descriptions, we discuss how the components are taken into account.

4 Analysis of GLE timing

4.1 Waiting time distribution

Between 1942 and September 2017, a total of 72 GLEs have been observed, resulting in an average rate of approximately 0.95 GLEs per year. As the observations during the first years were unreliable considering smaller GLEs, omitting the observations made during solar cycles 17 and 18 would result in a better estimate for the event rate: 67 GLEs during the approximately 62.5 years, i.e., 1.07 GLEs per year. However, as can be seen from Figure 2, the occurrence of GLEs is not a homogenous process throughout the solar cycle. Therefore, a more detailed analysis is needed in order to accurately model the GLE occurrence.

The red squares in Figure 3 show the waiting time distribution of the GLEs occurring in 1956–2012. The waiting times were calculated using the GLE onset times given in Table 1. The distribution seems to be exponential except for the shortest (less than 30 days) and longest (more than 700 days) waiting times. Many of the GLEs that occur in quick succession are produced in the same active region; an example of this are GLEs 65–67, occurring between October 28 and November 2, 2003, in the NOAA active region 10486. As the events from the same active region are not statistically

[5] Note that here, and in Sections 5 and 6 , the acronym ESP is used to denote a type of particle event, as opposed to the name of the fluence model used elsewhere in the article.

[6] We used the revised (July 1, 2015) International Sunspot Number (ISN; version 2.0) from the World Data Center SILSO, Royal Observatory of Belgium, Brussels, found online at http://www.sidc.be/silso/

Table 2. Spectral parameters of GLEs and their ESP counterparts. The uncertainties are estimated by varying the parameter of interest while holding the other parameters at their best-fit values.

GLE	Episode	J_0 (p/cm^2)	ΔJ_0 (p/cm^2)	γ_1	$\Delta\gamma_1$	γ_2	$\Delta\gamma_2$	R_0 (GV)	ΔR_0 (GV)
5	1	1.75E+08	1.59E+07	1.76	0.06	5.04	0.12	5.66E−01	3.49E−02
7	3	7.88E+08	7.96E+07	1.35	0.08	6.08	0.22	1.44E−01	5.50E−03
8	4	8.16E+05	9.42E+04	1.53	0.08	4.88	0.17	5.85E−01	3.93E−02
9	5	1.24E+08	1.36E+07	0.32	0.08	5.56	0.35	1.41E−01	5.70E−03
10	6	1.22E+08	1.41E+07	2.76	0.09	6.54	0.14	3.47E−01	1.97E−02
11	6	3.33E+07	4.11E+06	3.14	0.09	7.00	0.11	4.38E−01	2.84E−02
12	6	3.07E+07	3.68E+06	1.11	0.09	5.21	0.16	1.97E−01	1.08E−02
13	7	6.30E+08	7.21E+07	0.76	0.09	6.13	0.20	1.31E−01	4.20E−03
16	9	1.07E+07	1.48E+06	1.90	0.12	5.62	0.09	3.72E−01	2.38E−02
19	11	7.29E+06	8.17E+05	2.82	0.09	6.91	0.18	2.41E−01	1.30E−02
21	13	9.32E+07	1.21E+07	0.35	0.09	4.32	0.06	1.54E−01	8.00E−03
22	14	7.42E+06	7.77E+05	3.26	0.08	6.58	0.14	2.87E−01	1.63E−02
23	15	2.34E+08	2.82E+07	0.70	0.09	7.38	0.12	1.81E−01	6.30E−03
24	16	6.47E+10	7.50E+09	0.87	0.01	7.95	0.42	7.13E−02	1.00E−03
25	16	6.34E+06	7.19E+05	3.26	0.09	6.27	0.13	2.98E−01	1.94E−02
26	17	7.24E+06	9.04E+05	1.07	0.11	4.44	0.12	1.63E−01	8.50E−03
27	18	7.62E+06	6.21E+05	1.71	0.06	6.33	0.32	2.05E−01	7.70E−03
28	19	1.39E+06	1.10E+05	3.00	0.06	7.95	0.54	3.16E−01	1.96E−02
29	19	4.32E+06	4.15E+05	1.73	0.07	5.40	0.12	3.39E−01	2.54E−02
30	20	3.02E+06	2.92E+05	2.53	0.08	5.41	0.07	4.24E−01	2.87E−02
31	21	6.42E+06	4.54E+05	1.55	0.03	3.87	0.13	1.81E−01	8.60E−03
32	22	8.15E+09	8.47E+08	0.47	0.05	5.61	0.16	6.82E−02	2.30E−03
35	25	9.51E+04	5.87E+03	4.21	0.04	6.49	0.19	8.17E−01	9.74E−02
36	26	6.80E+08	4.45E+07	1.34	0.03	5.11	0.08	7.68E−02	1.80E−03
37	27	2.21E+05	1.73E+04	3.36	0.06	4.87	0.07	8.65E−01	1.42E−01
38	28	4.17E+05	4.38E+04	3.71	0.09	5.04	0.07	1.27E+00	2.06E−01
39	29	2.51E+07	1.65E+06	0.76	0.04	5.05	0.19	1.64E−01	5.80E−03
40	30	1.29E+07	1.16E+06	0.54	0.09	6.60	0.20	1.82E−01	5.50E−03
41	31	7.27E+07	6.52E+06	1.91	0.07	5.86	0.19	1.85E−01	7.10E−03
42	32	1.80E+05	2.23E+04	2.06	0.14	2.63	0.07	3.66E+00	1.24E+00
42ESP	32	2.03E+10	2.14E+09	-0.11	0.06	4.58	0.04	9.45E−02	3.00E−03
43	32	1.22E+09	1.27E+08	0.53	0.09	5.81	0.07	1.62E−01	5.30E−03
43ESP	32	9.09E+09	2.56E+08	0.91	0.02	4.43	0.04	8.44E−02	8.00E−04
44	32	1.09E+09	1.13E+08	1.23	0.09	7.25	0.16	1.35E−01	3.90E−03
45	32	4.42E+07	5.01E+06	2.18	0.10	5.65	0.06	3.85E−01	2.36E−02
46	33	3.85E+06	3.41E+05	0.97	0.07	5.53	0.23	2.20E−01	8.80E−03
47	34	1.13E+08	9.08E+06	0.55	0.12	4.31	0.09	1.37E−01	4.50E−03
48	34	5.58E+07	5.92E+06	0.80	0.08	4.91	0.06	1.83E−01	8.30E−03
49	34	4.69E+07	4.70E+06	0.33	0.07	5.72	0.13	1.83E−01	6.40E−03
50	34	7.66E+07	2.20E+06	0.42	0.02	4.98	0.18	1.43E−01	2.10E−03
51	35	8.36E+08	4.59E+07	0.97	0.22	5.14	0.12	1.05E−01	4.10E−03
52	35	2.52E+07	2.60E+06	2.18	0.09	5.98	0.11	2.36E−01	1.08E−02
53	36	8.62E+05	7.13E+04	3.12	0.06	6.12	0.21	3.50E−01	2.06E−02
54	37	1.97E+09	1.38E+08	0.46	0.06	6.91	0.42	9.51E−02	2.10E−03
55	38	8.15E+08	8.47E+07	0.28	0.09	5.38	0.09	1.16E−01	3.50E−03
56	39	8.98E+06	7.53E+05	1.31	0.07	6.51	0.55	1.96E−01	7.10E−03
57	39	1.64E+06	3.67E+04	1.92	0.01	7.46	0.41	2.02E−01	2.90E−03
58	40	2.10E+05	4.67E+03	2.98	0.01	5.27	0.34	6.77E−01	3.35E−02
58ESP	40	1.63E+04	4.00E+02	5.29	0.01	7.74	0.34	9.83E−01	5.96E−02
59	41	2.94E+09	2.91E+08	0.51	0.10	7.46	0.14	1.23E−01	3.00E−03
59ESP	41	6.01E+07	1.78E+06	3.24	0.05	7.85	0.29	2.26E−01	4.40E−03
60	42	5.22E+07	5.37E+06	1.39	0.09	5.69	0.08	2.60E−01	1.18E−02
61	42	8.39E+06	7.48E+05	1.85	0.07	5.02	0.14	2.37E−01	1.16E−02
62	43	2.14E+09	1.87E+08	0.24	0.07	6.67	0.31	9.34E−02	2.20E−03
62ESP	43	4.78E+08	1.06E+07	2.36	0.03	11.2	0.26	1.29E−01	1.30E−03
63	44	2.17E+07	1.85E+06	1.81	0.07	7.86	0.34	1.80E−01	5.80E−03

Table 2. (continued).

GLE	Episode	J_0 (p/cm^2)	ΔJ_0 (p/cm^2)	γ_1	$\Delta\gamma_1$	γ_2	$\Delta\gamma_2$	R_0 (GV)	ΔR_0 (GV)
64	45	5.06E+06	4.55E+05	2.36	0.07	6.70	0.33	2.25E−01	9.70E−03
65	46	8.44E+09	7.74E+08	0.01	0.08	6.48	0.25	8.88E−02	2.90E−03
65ESP	46	1.12E+08	3.17E+06	2.81	0.04	8.92	0.10	1.71E−01	2.90E−02
66	46	7.62E+07	1.71E+06	2.04	0.01	6.86	0.30	2.06E−01	3.20E−03
67	46	2.27E+06	1.92E+05	3.50	0.06	7.01	0.52	3.21E−01	1.70E−02
68	47	3.51E+07	1.09E+06	2.65	0.05	8.29	0.11	1.62E−01	2.80E−03
69	47	3.80E+08	2.87E+07	0.72	0.06	5.78	0.06	2.04E−01	6.90E−03
70	48	1.33E+08	1.39E+07	1.05	0.09	5.80	0.09	1.77E−01	6.60E−03
71	49	1.03E+07	1.10E+06	1.36	0.09	6.96	0.97	2.19E−01	7.90E−03

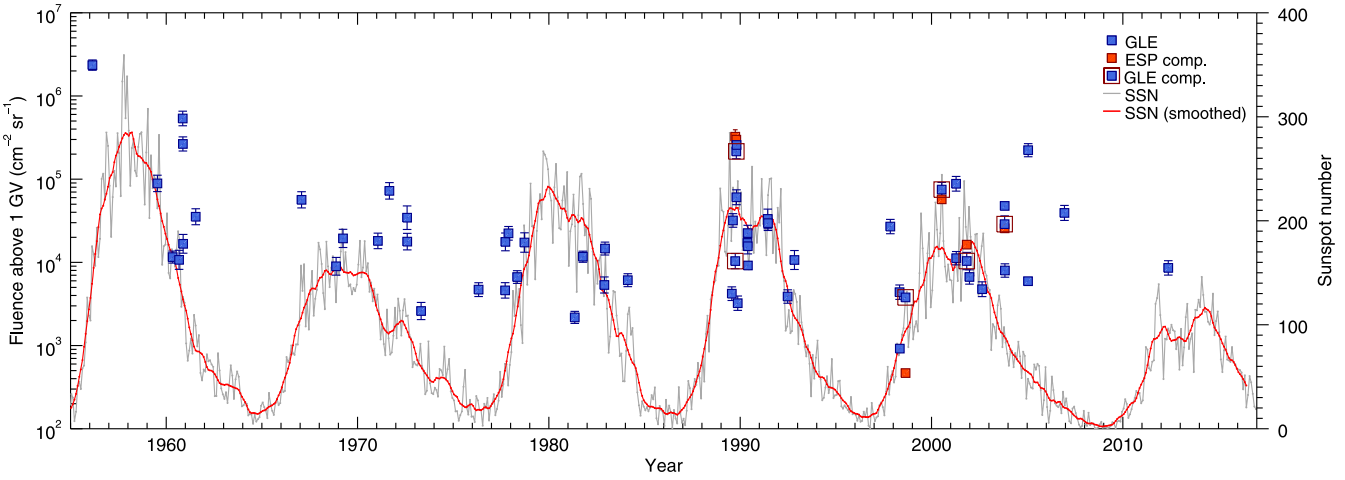

Fig. 2. Event-integrated >1 GV proton fluences (blue symbols) for the GLEs occurring in 1956–2012. Red squares around the symbols mark the GLE components of six events, coupled with their energetic storm particle components shown in red (see text). Monthly and 13-month smoothed monthly sunspot numbers are shown as the grey and red lines.

independent of each other, the occurrence of active regions capable of producing one or more GLEs is a better subject for analysis than the occurrence of individual GLEs. Thus, we grouped together all GLEs occurring in the same active region, resulting in 49 GLE episodes with one or more GLEs. The episode waiting times, calculated as the difference of the onset times of the first GLEs of both episodes, are shown as the blue squares in Figure 3. The exponential fit to waiting times less than 700 days, shown as the blue line, describes the data very well. Five out of the six waiting times greater than 700 days occur between the last event of the previous cycle and the first event of the following cycle (marked with extra squares in Fig. 3). The only exception is episode 3, on July 16, 1959, occurring 1049 days after the previous episode on August 31, 1956. The IGY-type NMs used during this time had lower statistics and time resolution compared to the NM64 introduced in the early 1960s (Stoker et al., 2000, and references therein). In addition, the number of NMs increased from only twelve during January 1957 to 51 by the end of the year (Shea and Smart, 2000). Therefore, one or more small GLEs may have occurred unobserved, resulting in an erroneous waiting time. Nonetheless, Figure 3 strongly suggests that considering the GLE episodes, each cycle consists of an active period with GLE episodes occurring as a Poisson process with a mean rate, λ of 0.00274 per day (1.002 per year)[7], and a quiet period with too few episodes to reasonably estimate a mean rate.

4.2 Normalized occurrence time

To study the occurrence of GLE episodes within a cycle in a better way, we calculated the normalized occurrence times of GLE episodes after the start of the corresponding solar cycle, which we take to be middle of the month with the lowest sunspot number, according to the following equation:

$$t_{norm} = \mu_d \cdot \frac{t_i - t_{min(i)}}{t_{min(i+1)} - t_{min(i)}}, \quad (4)$$

[7] As stated previously, GLE 72 is not included in the analysis. The waiting time between GLEs 71 and 72 is 1943 days, which would be a clear outlier in Figure 3, especially because both events occurred during the same solar cycle. Because the waiting time is longer than 700 days, it would not be included in the exponential fit, but the probabilities of each datapoint would change slightly. Thus, if GLE 72 was included in the analysis, the Poisson parameter for the GLE episode occurrence would be $\lambda = 0.00262\ \mathrm{d}^{-1} = 0.958\mathrm{a}^{-1}$.

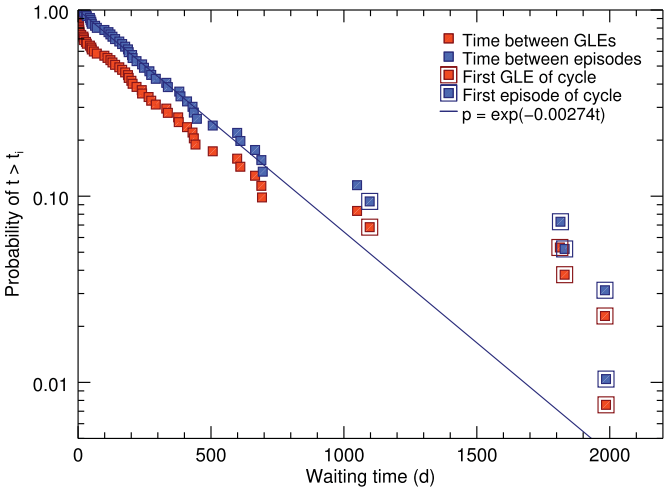

Fig. 3. Waiting time distribution of the GLEs (shown in red) and GLE episodes (shown in blue). The blue line is a fit to episode waiting times less than 700 days. The first GLEs and episodes of each cycle have been marked with extra squares.

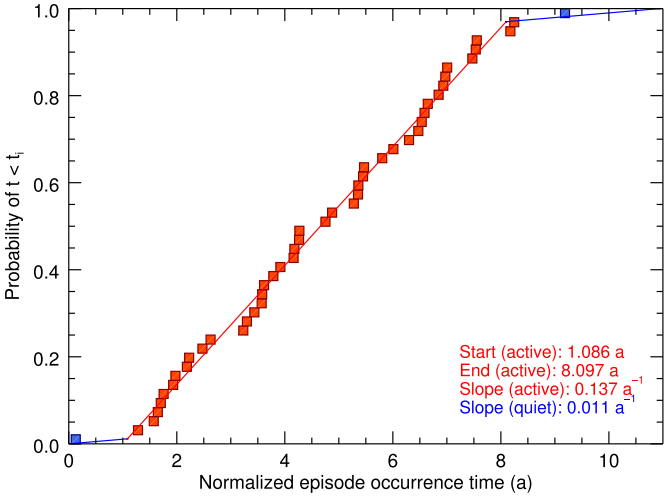

Fig. 4. Occurrence times of GLE episodes during a normalized solar cycle. The lines represent fits to the occurrence times during the active (red) and quiet parts (blue) of the cycle.

where $\mu_d = 10.93$ a is the average duration of the solar cycles 19–23, $t_{min(i)}$ the date of the cycle minimum before the episode, $t_{min(i+1)}$ the date of the cycle minimum after the episode and t_i the date of the episode. Figure 4 shows the cumulative distribution of the normalized occurrence times. From this figure it becomes clear that there are indeed two different levels of GLE activity within a cycle: most of the GLE episodes occur during and between the second and seventh years of the standard cycle, leaving very little activity to the first and the last three years of the cycle. More precisely, we assume that only the first and last points of the distribution constitute the quiet part of the cycle. The rest of the points, 46 out of 48 can be well fitted with a line (red line in Fig. 4). Normalized

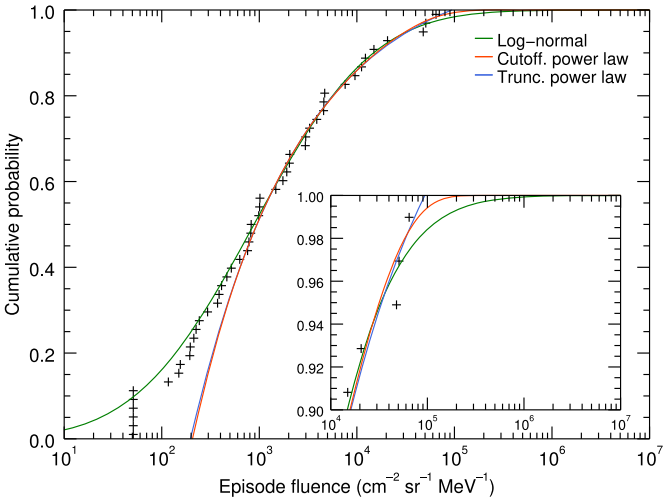

Fig. 5. Cumulative probability distribution of episode fluences for the 200–300 MeV energy channel, with the top 10% shown in greater detail in the inset.

occurrence time for the most recent GLE, on May 17, 2012, cannot be calculated because, as of this writing, cycle 24 is still underway. With the further assumption that the rate of occurrence during the quiet part in the beginning of the cycle is equal to the rate of occurrence during the quiet part in the end of the cycle (shown as blue lines in Fig. 4), we can calculate the starting and ending times of the active part, as well as the rate of occurrence of GLE episodes during the quiet part. The resulting durations for the quiet and active parts of the standard cycle are 3.923 a and 7.011 a, respectively. The rates of occurrence of GLE episodes are the slopes of the linear fits given in the figure multiplied by the total number of episodes (48) and divided by the number of cycles (5), resulting in $0.102\,\mathrm{a}^{-1}$ and $1.312\,\mathrm{a}^{-1}$ for the quiet and active parts, respectively. Note that the resulting value for the active part is higher than the value given in Section 4.1, which is also effectively calculated for the active part of the cycle.

5 Model 1

Our first model is a JPL-type proton fluence model which was originally developed as a part of the Interplanetary and Planetary Radiation Analysis Model for Human Spaceflight (IPRAM) project for the European Space Agency (ESA). After some small improvements, it was released as a part of the Space Radiation Expert Service Centre (R-ESC) on ESA's Space Situational Awareness (SSA) Space Weather (SWE) Service Network[8]. We utilized the set of Band-fit parameters and calculated differential fluence spectra for each individual GLE and ESP component using the equation

[8] The goal of the SWE network is to support users in mitigating the space weather effects while reducing costs and improving reliability of their systems. In addition to the R-ESC, the SWE network consists of four ESCs: Solar Weather, Heliospheric Weather, Ionospheric Weather and Geomagnetic Conditions. The R-ESC is available at http://swe.ssa.esa.int/space-radiation

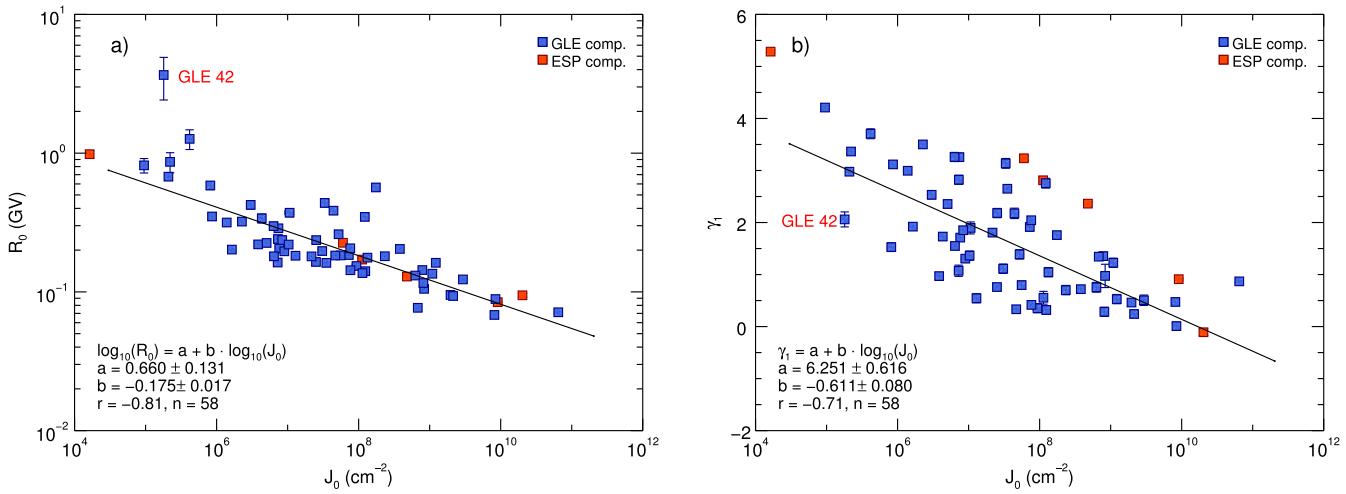

Fig. 6. (a) Parameter R_0 as a function of parameter J_0. GLEs are shown in blue and ESP components in red. Results of a linear fit in log-log-scale is shown in black. ESP components as well as GLE 42 are excluded from the fit. (b) Parameter γ_1 as a function of parameter J_0. The formatting is similar to a), but the fit is performed in log-lin-scale.

$$\frac{dJ}{dE}(E) = \frac{J(>R_1) - J(>R_2)}{E_2 - E_1}, \tag{5}$$

where $J(>R_i)$ is the integral fluence calculated with the Band function and R_i is the rigidity corresponding to the kinetic energy E_i. We used the reference energies of channels 3–10 of the SEPEM model (Jiggens et al., 2012), plus additional four logarithmically spaced channels to obtain an energy range from about 10 MeV to 1 GeV. The eight small GLEs, for which the Band fits were not performed, were assumed to have a fluence equal to the smallest fluence in each energy channel. Fluence spectra for the multi-GLE episodes were calculated by summing over the individual GLE spectra, as was also done in the case of separately analyzed GLE and ESP components.

The cumulative probability distribution of episode integrated fluences for each individual channel was analyzed by fitting three functions: log-normal distribution, truncated power law, and exponentially cut-off power law, given by the following equations, respectively:

$$F(\phi) = \frac{1}{2}\left[1 + \mathrm{erf}\left(\frac{\log_{10}(\phi) - \mu}{\sigma\sqrt{2}}\right)\right] \tag{6a}$$

$$F(\phi) = \frac{\phi_{min}^{-b} - \phi^{-b}}{\phi_{min}^{-b} - \phi_{\max}^{-b}} \tag{6b}$$

$$F(\phi) = 1 - \frac{\phi^{-\gamma}\exp\left(\frac{\phi_{low}}{\phi_{lim}}\right)}{\phi_{low}^{-\gamma}\exp\left(\frac{\phi}{\phi_{lim}}\right)}, \tag{6c}$$

where $F(\phi)$ is the probability of an episode fluence being lower than the fluence ϕ, μ and σ are the mean and standard deviation of $\log_{10}(\phi)$, b and γ are power law exponents, ϕ_{min} and ϕ_{low} are parameters related to the lower limit of the distribution, and ϕ_{max} and ϕ_{lim} parameters related to the upper limit of the distribution. All parameters in equations (6a)–(6c) are fitted to the binned distribution, not calculated directly from the sample.

Figure 5 shows the fluence distribution and the three fit functions for the energy channel of 200–300 MeV as an example. The inset shows the top 10% probability in greater detail. As can be seen from the figure, the log-normal fit (shown in green), while describing the data well for moderate fluences, has a long tail in the very high fluences. This can result in over-estimation of mission fluences at high confidence levels in our model. On the other hand, the truncated power law distribution (shown in blue) has a maximum value close to the highest observed fluence, which implies that the highest possible fluence has been already measured, probably resulting in under-estimation of fluences. Therefore, we select the cut-off power law (shown in red) as a compromise between the two cases.

6 Model 2

6.1 Distribution of parameters

The principle of our second proton fluence model is to model the actual spectral shape of GLEs instead of the fluences in separate energy channels. To achieve this we first analyse the relationships between the spectral parameters and find out how they are distributed. Figure 6(a) presents the relationship between the parameters J_0 and R_0. Blue squares mark the GLEs and GLE components of those events with separately analysed GLE and ESP components, while the ESP components are shown in red. As the ESP components may result from a different physical process than their GLE counterparts, we will treat them separately in Section 6.4. GLE 42 (29 September 1989), which is marked in the plot, has the largest value for R_0 (and also the smallest one for γ_2) of the whole set of parameters, and is clearly an outlier. A linear fit was performed in log-log-scale (implying a power law dependence), omitting the ESP components and GLE 42. The results of the fit are shown in black. With the correlation coefficient $r = -0.81$ and sample size $n = 58$, the probability that the correlation occurs by chance is very small ($p \ll 0.001$), and thus we can say that the parameter R_0 is statistically significantly correlated with J_0. Similarly, Figure 6(b) presents the relationship between the parameters γ_1 and J_0. In this figure the linear fit

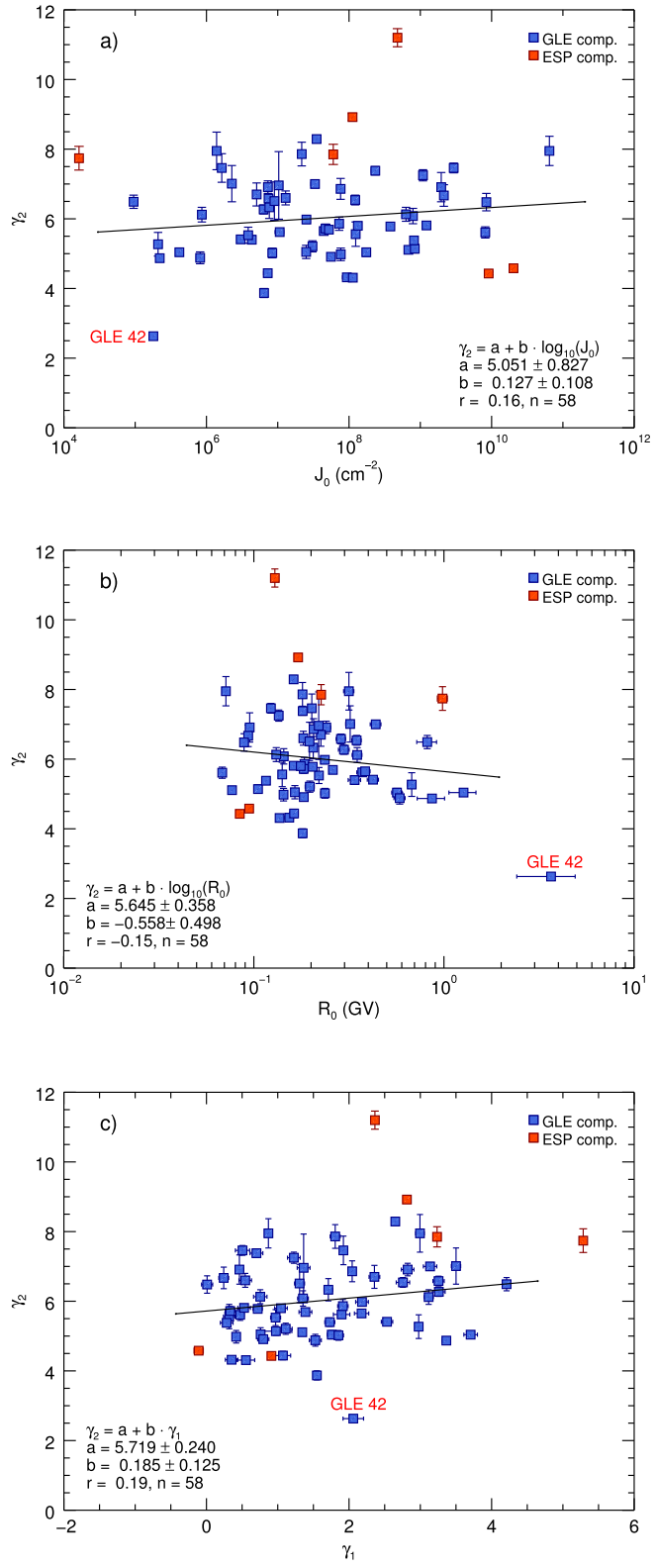

Fig. 7. Parameter γ_2 as functions of J_0 (a), R_0 (b) and γ_1 (c). The formatting in each figure is similar to Figure 6.

is performed in log-lin-scale, implying a logarithmic dependence. The correlation coefficient is now $r = -0.71$, which again gives a very small probability ($p \ll 0.001$) that the correlation occurs by chance. This means that there is also statistically significant correlation between the parameters γ_1 and J_0.

Figures 7(a)–7(c) show the parameter γ_2 as a function of J_0, R_0 and γ_1, respectively. The formatting in each figure is similar to the previous figure. In Figures 7(a) and (b) the linear fits were performed in log-lin-scale. In none of the three cases is the correlation significant at 95% level. Although non-correlation does not necessarily imply statistical independence, we make that assumption for simplicity, i.e., we assume that the parameter γ_2 is independent from the other parameters. Thus, we have two independent parameters, J_0 and γ_2, and two parameters, R_0 and γ_1, that depend upon the value of J_0.

In the following we show that the parameters J_0 and R_0 are distributed log-normally and the parameters γ_1 and γ_2 normally. Figure 8(a) presents the cumulative distribution function (CDF) of the logarithm of the independent parameter J_0 shown in red. The Gaussian CDF, shown in blue, is calculated with the sample mean and variance of $\log_{10}(J_0)$. We utilize the Lilliefors test (Lilliefors, 1967; Dallal and Wilkinson, 1986) to see whether or not $\log_{10}(J_0)$ is indeed distributed normally. The test statistic, $D_{\log_{10}(J_0)} = 0.071$, equals the largest discrepancy between the empirical CDF and the Gaussian CDF. For 5% confidence level and a sample size of $n = 58$, the critical value for the test statistic would be $D_{crit} = 0.116$. As the resulting test statistic is smaller than the critical value, we can safely assume $\log_{10}(J_0)$ to be normally distributed. The CDF of the other independent parameter, γ_2, is shown in Figure 8(b), with similar formatting as in Figure 8(a). Again, we utilize the Lilliefors test, and with the test statistic, $D_{\gamma_2} = 0.081 < D_{crit}$, we can assume that the parameter γ_2 is normally distributed.

To find information about the distribution of the dependent parameters, we first have to remove the J_0-dependency. This is done via the following equations:

$$\log_{10}(R_0)' = \log_{10}(R_0) - 0.660 + 0.175 \cdot \log_{10}(J_0) \quad (7a)$$

$$\gamma_1' = \gamma_1 - 6.251 + 0.611 \cdot \log_{10}(J_0), \quad (7b)$$

where the numerical factors are taken from the linear fits shown in Figures 6(a) and 6(b). Figures 9(a) and (b) show the CDFs of the "residual" parameters $\log_{10}(R_0)'$ and γ_1', respectively, with similar formatting as in Figure 8. For the test statistics we get $D_{\log_{10}(R_0)'} = 0.110$ and $D_{\gamma_1'} = 0.059$. Both of these values are again smaller than the critical value, and therefore we can assume that the parameters $\log_{10}(R_0)'$ and γ_1' are also distributed normally.

To summarise, we find that the parameters of the GLEs are distributed according to the following equations (here $N(\mu, \sigma^2)$ denotes a normal distribution with mean μ and variance σ^2):

$$D(\log_{10}(J_0)) = N(\mu = 7.589, \sigma^2 = 1.540), \quad (8a)$$

$$D(\log_{10}(R_0)) = N(\mu = 0, \sigma^2 = 0.025) + 0.660 - 0.175 \cdot \log_{10}(J_0), \quad (8b)$$

$$D(\gamma_2) = N(\mu = 6.017, \sigma^2 = 1.023), \quad (8c)$$

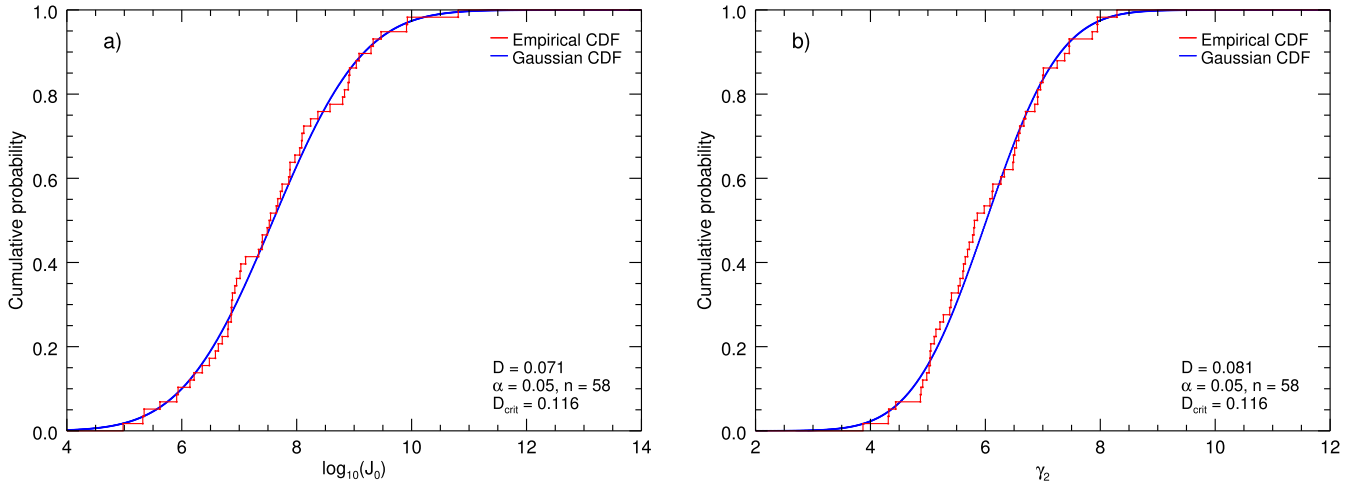

Fig. 8. (a) Cumulative distribution function of the logarithm of the parameter J_0, shown in red. A Gaussian CDF with the mean and variance calculated from the data is shown in blue. The test statistic D is the largest discrepancy between the empirical CDF and Gaussian CDF. (b) Similar to a), but for the parameter γ_2.

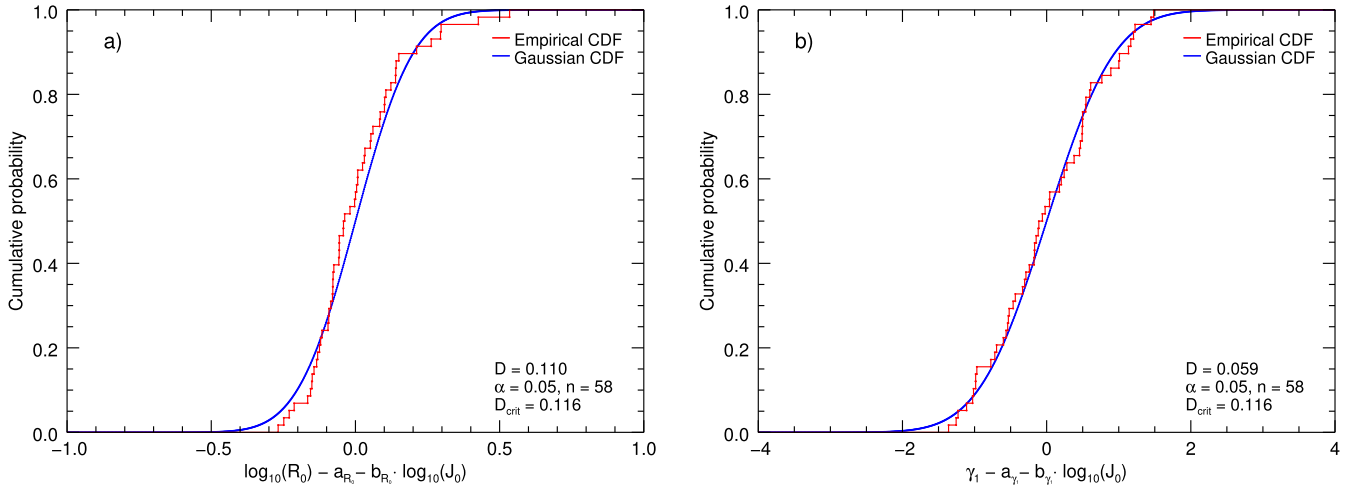

Fig. 9. Similar to Figure 8, but for the "residual" parameters $\log_{10}(R_0)'$ (a) and γ_1' (b).

$$D(\gamma_1) = N(\mu = 0, \sigma^2 = 0.553) + 6.251 - 0.611 \cdot \log_{10}(J_0). \quad (8d)$$

6.2 Small GLEs

In the first model, we considered the small GLEs as having fluences equal to the smallest fluence of the GLEs with Band-fits in each energy channel, but here we adopt a more detailed approach. In addition to the dataset of GLE spectral parameters we have been using, we can utilize a similar dataset but for so-called sub-GLEs, i.e., large SEP events with increases of protons above 300 MeV, but not with sufficient intensities to be detected with ground level neutron monitors. The spectral parameters (and their uncertainties) for sub-GLEs occurring in solar cycles 20–22 are given in Table 3. The parameters for the sub-GLEs occurring in cycles 23 and 24 are listed in Vainio et al. (2017). Figure 10 shows the response (number of counts measured) of a high-latitude NM, ΔN, (in arbitrary units) for both GLEs and sub-GLEs, calculated with the equation

$$\Delta N = \int_1^\infty \frac{\mathrm{d}}{\mathrm{d}R} J(>R) \cdot y(R) \mathrm{d}R, \quad (9)$$

where $y(R)$ is the neutron monitor yield function of Clem and Dorman (2000). GLEs are shown in blue and sub-GLEs in red. The observations of sub-GLEs were performed with IMP-8/GME from October 1973 to 1986 and with GOES/HEPAD after 1986. IMP-8/GME had a lower background rate than GOES/HEPAD, and detected a few smaller events which fall below the lower limit of the figure, but as they are outside the range of interest, we decided to omit those and show only the events with $\Delta N > 10$, which seems to be approximately the low

Table 3. Spectral parameters of sub-GLEs and an ESP counterpart. The uncertainties are estimated by varying the parameter of interest while holding the other parameters at their best-fit values.

Year	Month	Day	J_0 (p/cm^2)	ΔJ_0 (p/cm^2)	γ_1	$\Delta\gamma_1$	γ_2	$\Delta\gamma_2$	R_0 (GV)	ΔR_0 (GV)
1973	11	3	5.14E+05	2.40E+04	1.60	0.03	7.04	0.26	1.20E−01	2.00E−03
1974	9	19	2.19E+04	1.14E+03	4.11	0.05	4.66	0.12	9.90E−01	1.36E−01
1974	9	24	9.06E+06	4.20E+05	0.78	0.04	4.92	0.02	1.82E−01	4.00E−02
1974	11	5	1.18E+06	6.00E+04	1.70	0.03	7.01	0.11	1.39E−01	3.00E−03
1975	8	21	8.02E+05	3.70E+04	0.96	0.03	8.83	0.56	1.04E−01	1.00E−03
1975	8	22	4.38E+06	2.00E+05	0.61	0.03	5.74	0.40	9.80E−02	1.00E−03
1976	8	22	2.85E+06	1.40E+05	1.18	0.03	9.03	0.97	8.80E−02	1.00E−03
1978	2	13	1.03E+11	4.57E+09	0.01	0.02	10.90	0.27	3.28E−02	3.00E−04
1978	4	11	2.10E+06	9.53E+04	2.09	0.02	7.01	0.30	1.36E−01	3.80E−03
1978	4	19	1.66E+08	7.75E+06	0.28	0.02	11.00	0.78	6.85E−02	1.10E−03
1978	4	28	1.23E+10	4.87E+08	−0.26	0.01	4.56	0.07	3.93E−02	7.00E−04
1978	4	28ESP	7.72E+11	3.51E+10	−0.67	0.02	9.11	0.17	2.83E−02	2.00E−04
1979	8	18	5.26E+09	2.46E+08	0.32	0.02	5.19	0.14	4.35E−02	6.00E−04
1979	9	15	3.19E+09	1.46E+08	0.05	0.02	10.80	0.40	5.46E−02	6.00E−04
1981	4	24	5.06E+07	2.23E+06	1.50	0.02	5.88	0.08	7.50E−02	1.70E−03
1981	4	30	4.99E+07	2.27E+06	0.79	0.03	7.84	0.38	1.01E−01	2.30E−03
1981	10	8	8.61E+06	3.96E+05	1.99	0.02	4.41	0.12	9.63E−02	2.60E−03
1982	2	1	1.80E+09	7.94E+07	0.43	0.02	7.31	0.16	4.86E−02	7.00E−04
1982	11	22	9.40E+05	4.39E+04	2.19	0.02	8.75	0.46	9.60E−02	1.70E−03
1982	12	17	1.02E+06	4.56E+04	2.19	0.02	5.04	0.02	1.77E−01	6.00E−03
1982	12	19	3.03E+06	1.35E+05	1.95	0.02	6.60	0.09	1.09E−01	2.30E−03
1984	4	25	4.53E+09	2.00E+08	0.51	0.02	6.07	0.06	5.80E−02	1.00E−03
1985	1	22	3.09E+06	1.40E+05	1.08	0.02	9.23	0.45	9.50E−02	1.00E−03
1985	4	24	2.40E+04	1.20E+03	4.08	0.04	6.83	0.21	3.64E−01	2.00E−02
1985	7	8	5.17E+06	2.30E+05	1.27	0.02	7.05	0.16	9.04E−02	1.50E−03
1985	7	17	1.83E+06	8.00E+04	0.09	0.03	4.35	0.30	1.74E−01	4.30E−03
1986	2	6	1.16E+07	4.00E+05	1.03	0.02	10.20	0.60	1.43E−01	2.00E−02
1986	2	7	1.05E+06	5.00E+04	2.75	0.03	8.48	0.29	1.55E−01	4.00E−03
1986	2	14	4.70E+05	2.20E+04	3.36	0.03	8.58	0.37	1.53E−01	3.00E−03
1989	5	20	1.91E+05	5.00E+03	2.51	0.02	3.59	0.29	8.46E−01	7.20E−02
1989	8	12	9.84E+07	4.00E+06	2.44	0.07	11.00	1.30	1.38E−01	2.00E−03
1989	10	29	2.24E+07	7.00E+05	0.63	0.03	4.82	0.27	1.30E−01	2.00E−03
1989	11	30	1.15E+15	5.17E+13	-3.65	0.03	12.00	2.02	2.05E−02	1.00E−04
1991	3	23	3.80E+07	1.80E+06	3.04	0.09	8.89	1.09	1.84E−01	4.00E−03
1991	5	13	3.24E+06	1.00E+05	2.28	0.02	11.90	2.30	1.48E−01	2.00E−03
1991	6	4	5.24E+08	1.50E+07	0.63	0.01	11.90	0.10	1.02E−01	1.00E−03
1991	10	30	7.34E+06	2.10E+05	0.98	0.02	5.54	0.32	1.95E−01	4.00E−03
1992	3	7	5.43E+06	2.48E+05	0.15	0.02	4.19	0.08	1.59E−01	5.00E−03

limit for GOES/HEPAD. There is a large overlap in the ΔN values of GLEs and sub-GLEs, although in reality the sub-GLEs were not observed by NMs with the geomagnetic cutoff rigidity above 1 GV. One reason for the overlap could be that the sub-GLEs were fitted with only satellite data, not taking into account that the neutron monitors did not detect them.

The two dashed lines in Figure 10 show the highest ΔN from sub-GLEs and the lowest ΔN from GLEs, and the events with fluences between these values are marked with square symbols. We select these events to represent the eight GLEs for which the Band-fitting was not performed. This selection is a good balance between assuming that all the small GLEs have fluences equal to the smallest fitted GLE in each channel, and assuming that the small GLEs are similar to the other GLEs.

For simplicity and brevity, we assume that the parameters of the selected GLEs and sub-GLEs behave similarly as the parameters of the GLEs, i.e., $\log_{10}(J_0)$ and γ_2 are normally distributed independent variables, and $\log_{10}(J_0)$ and γ_1 are normally distributed variables which depend linearly upon the value of $\log_{10}(J_0)$. We find that the parameters of the small GLEs are distributed according to the following equations:

$$D(\log_{10}(J_0)) = N(\mu = 7.397, \sigma^2 = 2.257), \tag{10a}$$

$$D(\log_{10}(R_0)) = N(\mu = 0, \sigma^2 = 0.022) + 0.714 - 0.195 \cdot \log_{10}(J_0), \tag{10b}$$

$$D(\gamma_2) = N(\mu = 6.374, \sigma^2 = 3.660), \tag{10c}$$

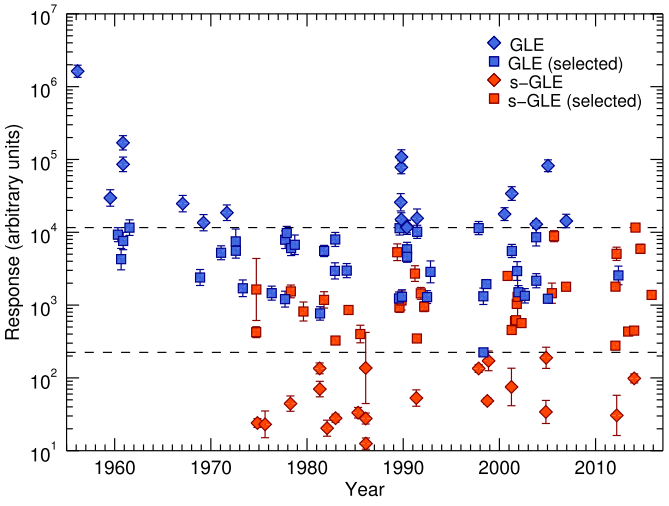

Fig. 10. Response (number of counts measured) of a NM with cutoff at 1 GV in arbitrary units. GLEs are shown in blue and sub-GLEs in red. Squares indicate the events chosen to represent the smallest GLEs.

$$D(\gamma_1) = N(\mu = 0, \sigma^2 = 0.753) + 5.972 - 0.582 \cdot \log_{10}(J_0). \quad (10d)$$

6.3 Unphysical parameters

As can easily be seen, the spectral parameter distributions presented in equations (8) and (10) also allow for unphysical combinations of parameters. Therefore care has to be taken to discard unphysical values when simulating the spectra. Firstly, if $\gamma_1 > \gamma_2$, R_1 in equation (1) has a negative value, which obviously is unphysical. Secondly, γ_1 and γ_2 are drawn from normal distributions, and may therefore have any real values. If γ_1 or γ_2 has a negative value, the corresponding power law index in equation (1) will be positive. As the integral spectrum must be strictly decreasing, this may result in an unphysical spectrum. If we look at the derivative of the Band function,

$$\frac{\mathrm{d}}{\mathrm{d}R}(J(>R)) = \begin{cases} -J_0 R^{-\gamma_1 - 1}\left[\gamma_1 \exp\left(-\frac{R}{R_0}\right) + \frac{R}{R_0}\exp\left(-\frac{R}{R_0}\right)\right], & R < (\gamma_2 - \gamma_1)R_0 \equiv R_1 \\ -J_0 \gamma_2 R_1^{\gamma_2 - \gamma_1} \exp\left(-\frac{R_1}{R_0}\right) R^{-\gamma_2 - 1}, & R \geq R_1 \end{cases}, \quad (11)$$

we see that the derivative has a zero at $R_z = -\gamma_1 R_0$. This means that in the cases where $\gamma_1 < 0$ but $\gamma_2 > 0$, the Band function is strictly decreasing when $R > R_z$. As we only consider energies above 10 MeV (rigidities above 0.137 GV) in our model, we decide to allow negative values for γ_1 if $R_z < 0.137$GV.

6.4 ESP components

Since the launch of IMP-4 in May 1967, 54 GLEs have been observed. The ESP components were found to exist for six out of the 54 events, i.e., for 11.1% of the events. Therefore, in our model, we make the simple assumption that each simulated event has a probability of 11.1% to have an additional ESP component. Going back to Figures 6 and 7, we see that five of the six ESP components have values of $\log_{10}(J_0)$ above the average value of $\mu_{\log_{10}(J_0)} = 7.589$ of GLEs. In addition, all of the γ_1-values for the ESP components are well above the γ_1 vs. J_0 line fitted for the GLEs. These properties imply high fluences for the lowest rigidities, which rapidly decrease with increasing rigidity, implying a soft spectrum. This is expected, as the ESP events are caused by particle acceleration or trapping in an interplanetary shock passing the observer. Still, the sample of six ESP events does not provide enough statistical significance for a proper analysis, and therefore we will simply model them similarly as the GLE events.

6.5 GLE episodes

In addition to the occurrence rate of the GLE episodes, we need to model the number of individual GLEs in each episode. The blue bars in Figure 11 show the proportion of episodes with the corresponding number of GLEs. Statistical errors are shown with the orange error bars. We compare this distribution with three common discrete probability distributions: (shifted) geometric, logarithmic and zero-truncated Poisson, shown in black, red and green, respectively. The following equations relate the expected number of events per episode, $E[X] = 1.367$, to the parameter, p_i, of the distributions:

$$E[X] = \frac{1}{p_g} \quad (12a)$$

$$E[X] = \frac{-1}{\ln(1 - p_l)} \frac{p_l}{1 - p_l} \quad (12b)$$

$$E[X] = \frac{p_p e^{p_p}}{e^{p_p} - 1}, \quad (12c)$$

where p_g, p_l and p_p are the parameters for geometric, logarithmic and zero-truncated Poisson distributions, respectively. All of these distributions describe the data at least reasonably, but we select the logarithmic distribution with $p = 0.449$ for our model since it resembles the observed numbers most closely.

6.6 Simulation procedure

The procedure for simulation of mission-integrated fluences is presented as follows:

- Draw the number of GLE episodes, N_{ep}, occurring during the mission from either $P(\lambda = 1.002 \cdot t)$ (one-component model) or $P(\lambda = 1.312 \cdot t_a + 0.102 \cdot t_q)$ (two-component model), where P denotes the Poisson distribution and t_a and t_q are the mission durations (in years) during the active and quiet parts of the solar cycle, respectively.
- For each episode, draw the number of GLE events per episode, N_{GLE}, from $L(p = 0.449)$, where L denotes the logarithmic distribution.

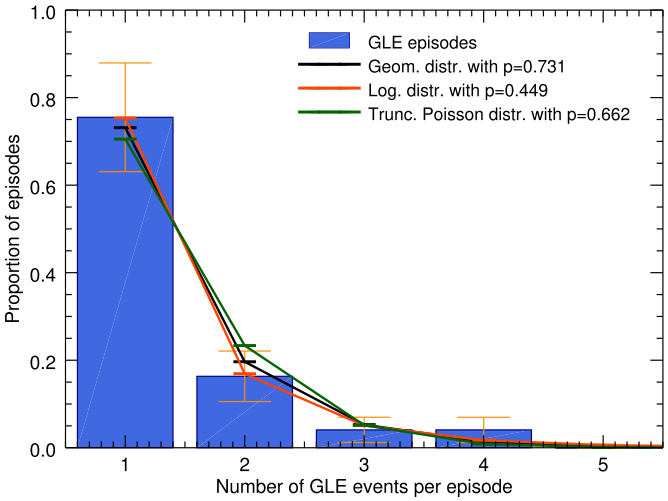

Fig. 11. Distribution of the number of GLEs per episode. Geometric, logarithmic and zero-truncated Poisson distributions shown for comparison (in black, red and green, respectively).

- $\frac{8}{67} \approx 11.9\%$ of the total number of GLEs are assumed to be small.
- $\frac{6}{54} \approx 11.1\%$ of the remaining (non-small) GLEs are assumed to have an ESP component.
- For each normal GLE and ESP component, draw the spectral parameters according to equations (8a)–(8d). If the resulting spectra is unphysical, draw the parameters again.
- For each small GLE, draw the spectral parameters according to equations (10a)–(10d). If the resulting spectra is unphysical, draw the parameters again.
- For each GLE and ESP, calculate the fluences for specified rigidities / energies using equations (1) and (5).
- Calculate the sum of the fluences of separate events in each rigidity / energy to get mission-integrated fluences.
- Repeat previous items for a large number of times to get the desired statistical accuracy.

7 Comparison of models

Figure 12(a) shows mission integrated differential fluence spectra for 50% and 95% confidence levels, calculated with one-component versions of both models, i.e., using a single Poisson parameter for GLE episode occurrence as presented in Section 4.1. Mission duration was one year. Model 1 is shown in blue and model 2 in red, and the confidence levels are shown with plus signs (50%) and crosses (95%). Here, and in the following comparisons, we repeat the simulations for $N = 1 \cdot 10^5$ times and sort the simulated fluences by ascending fluence values in each energy channel. The $[(\mathrm{CL}/100) \cdot N]$-th value for each energy is presented as the spectrum at confidence level CL%. The 50% confidence spectra in Figure 12(a) are of similar shape, but show a difference of factor of about 2–3. The 95% confidence spectra have slightly different shapes with model 1 showing a slight "bump" at ~50 MeV and decreasing more quickly at higher energies. Also of note is the fact that for 50% confidence, model 2 has higher fluences over the whole energy range, whereas for 95% confidence model 1 has higher fluences except for the energies above ~300 MeV.

With similar formatting, Figure 12(b) shows mission integrated differential spectra, calculated with the two-component versions of the models, i.e., using different Poisson parameters for active solar period and quiet solar period. The simulated mission had a duration of six years during solar active time and three years during solar quiet time. Here, model 1 has higher fluences for energies below about 140 MeV for both confidence levels. For the highest energies, model 2 is slightly higher for 50% confidence and model 1 for 95% confidence. The bump of model 1 at 95% confidence at about 50 MeV is more pronounced than in Figure 12(a), making the shape of the spectrum a bit unusual.

Figure 13(a) shows the probability of exceeding a mission integrated fluence for 2-year and 6-year missions at 200–300 MeV, calculated with the one-component versions of both models. The probability curves do not start at $P = 1.0$ because there is a finite probability for a mission to have no GLEs occurring during its duration, thus also having zero fluence. For a 2-year mission this chance is 0.135 and for a 6-year mission 0.002. The probability curves for the two models clearly have different shapes; for both the lowest and the highest fluences, model 1 gives a lower probability of exceeding. Only in the middle part, from about $3 \cdot 10^4\,\mathrm{cm^{-2}sr^{-1}\,MeV^{-1}}$ to $1 \cdot 10^5\,\mathrm{cm^{-2}sr^{-1}\,MeV^{-1}}$ for a 2-year mission and from about $6 \cdot 10^4\,\mathrm{cm^{-2}sr^{-1}\,MeV^{-1}}$ to $1.5 \cdot 10^5\,\mathrm{cm^{-2}sr^{-1}\,MeV^{-1}}$ for a 6-year mission, model 1 gives a higher probability. For the very highest fluences, the difference is quite large: the probability of exceeding a fluence of $3 \cdot 10^5\,\mathrm{cm^{-2}sr^{-1}\,MeV^{-1}}$ is larger for a 2-year mission simulated with model 2 than for a 6-year mission simulated with model 1.

The probabilities of exceeding worst case fluences presented in Figure 13(b) show very similar behaviour as the cumulative fluences in Figure 13(a). Here, model 1 gives higher probability of exceeding for fluences between about $10^3\,\mathrm{cm^{-2}sr^{-1}\,MeV^{-1}}$ and $10^4\,\mathrm{cm^{-2}sr^{-1}\,MeV^{-1}}$ for both 2 and 6 year missions. Again, for the very high fluences, the probability of exceeding is higher for a 2-year mission simulated with model 2 than for a 6-year mission simulated with model 1.

Figures 14(a) and (b) present comparisons of our two models with the SEPEM model and the ESA's Space Environment Information System (SPENVIS)[9] implementation of ESP and JPL models. The figures show mission integrated fluence spectra at 95% confidence for a 2 year mission (a) and a 7 year mission, (b). The SEPEM model agrees best with our models, the spectrum lying between our models for energies below 70 MeV, and falling below both of our models above 70 MeV, for both mission durations. The JPL model shows a slightly harder spectrum, which agrees with our models for low energies but is higher by a factor of about 3–5 for energies above 100 MeV. The ESP model shows the worst agreement, being clearly above both of our models for all energies.

Finally, in Figure 15 we compare the total fluence averaged over the years 1956–2012 to a "mission" simulated with our second model. The black curve, which shows the

[9] http://www.spenvis.oma.be

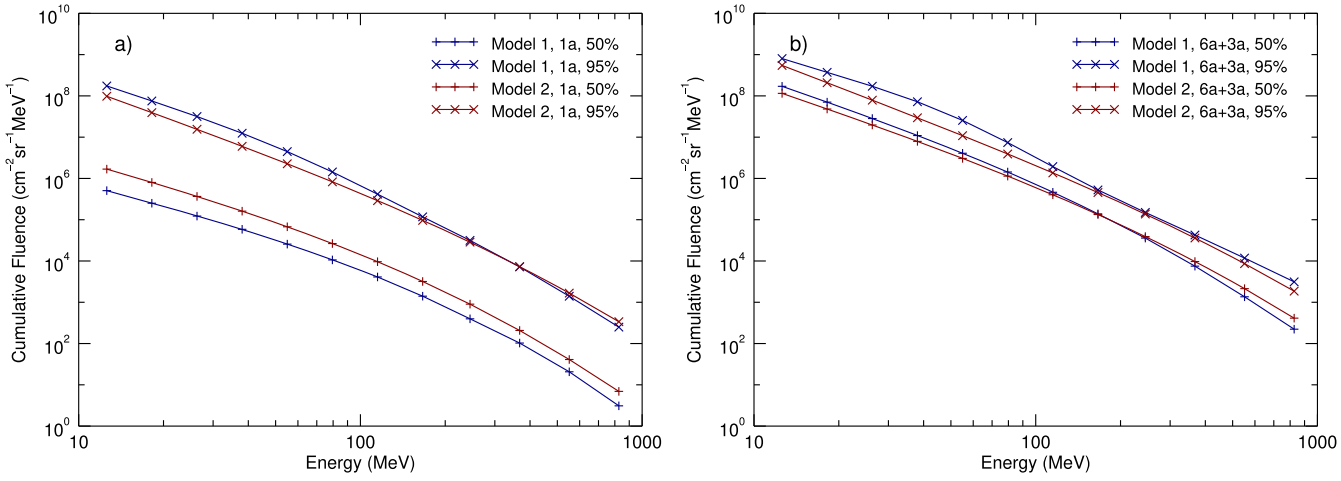

Fig. 12. (a) Mission integrated differential fluence spectra calculated with one-component versions of model 1 (in blue) and model 2 (in red), for one year mission, at 50% (plus signs) and 95% (crosses) confidence level. (b) Similar to (a), but calculated with two-component models, for a mission of 6 years during solar active time and 3 years during solar quiet time.

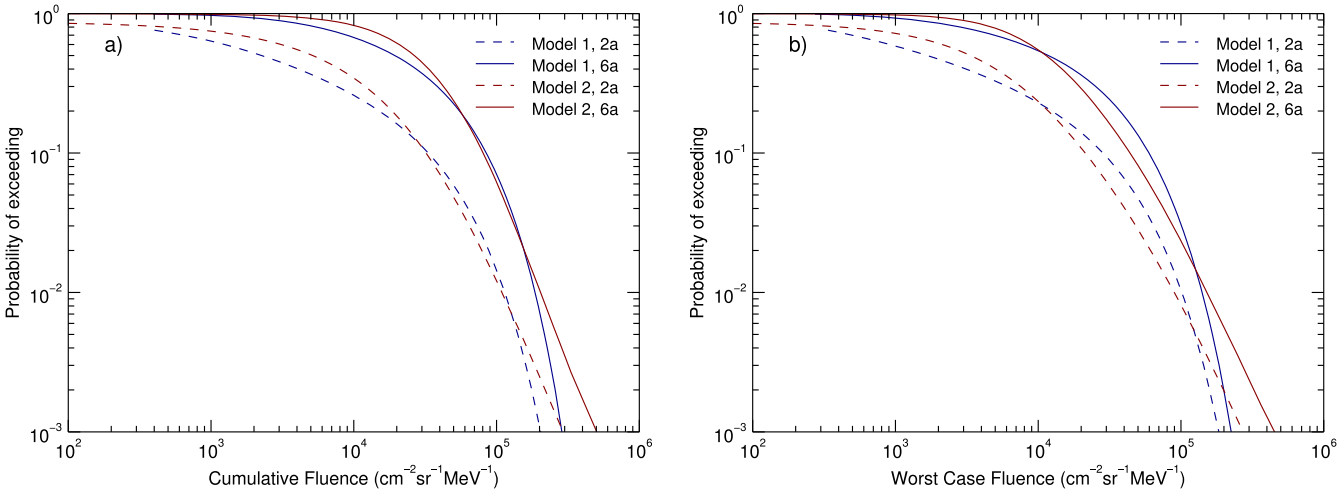

Fig. 13. (a) Probability of exceeding a cumulative fluence for the 200–300 MeV energy channel, calculated with one-component version of both models for two different missions. Model 1 is shown in blue and model 2 in red. 2-year mission is marked with dashed lines and 6-year mission with solid lines. (b) Probability of exceeding a worst-case fluence for the 200–300 MeV energy channel, with similar formatting as in (a).

total fluence from GLEs, calculated with the Band fits and averaged over the time interval, is similar to the blue curve in Figure 2 of Kovaltsov et al. (2014), except for a change of units to directional fluences. The orange curve shows the exponent-over-rigidity solar proton fluence spectrum averaged over 1954–2008 (Reedy 2012). Using the normalized solar cycle shown in Figure 4, we modeled the 1956–2012 time interval as 37 years of solar active time and 20 years of solar quiet time. The blue and red curves show the results, simulated with the second model and averaged over time, for 30% and 90% confidence levels, respectively. The 90% confidence spectrum is very close to the total GLE fluence at low energies, overestimating the fluence by an increasing amount above 100 MeV. The 30% confidence spectrum underestimates the GLE fluence at low energies, but gives a better estimation at energies above 100 MeV.

8 Summary and discussion

We have presented two new statistical models of high energy solar proton fluences. Both models are based on GLE fluence spectra observed with both satellites and ground-based neutron monitors during the solar cycles 19–24, but utilize different modeling methodologies. In the first methodology, we calculate mission-integrated integral fluences for certain energies from Band-function fits and model their distributions with exponentially cut-off power law functions. In the second methodology, we model the spectral parameters as two independent and two dependent, normally distributed variables, thus modeling the spectral shape itself. The results from the two models agree well except for short missions at low confidence levels. There is also reasonable agreement between our models and three commonly used

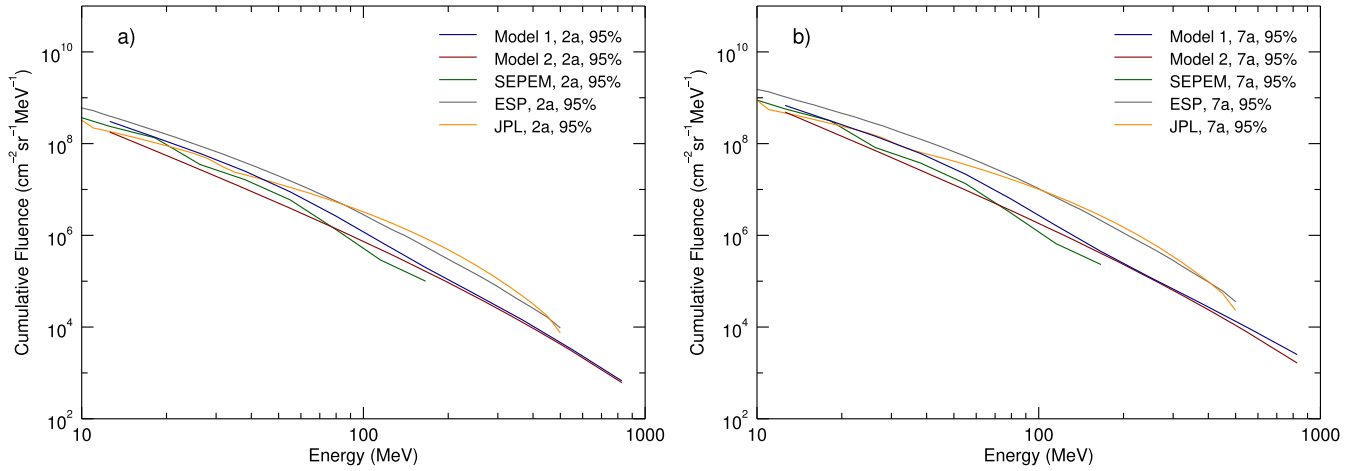

Fig. 14. (a) Mission integrated differential fluence spectra calculated for 2 year missions with 95% confidence, for one-component versions of our model 1 (blue), model 2 (red), SEPEM model (green), ESP model (gray) and JPL model (orange). (b) Similar to a), but for 7 year missions.

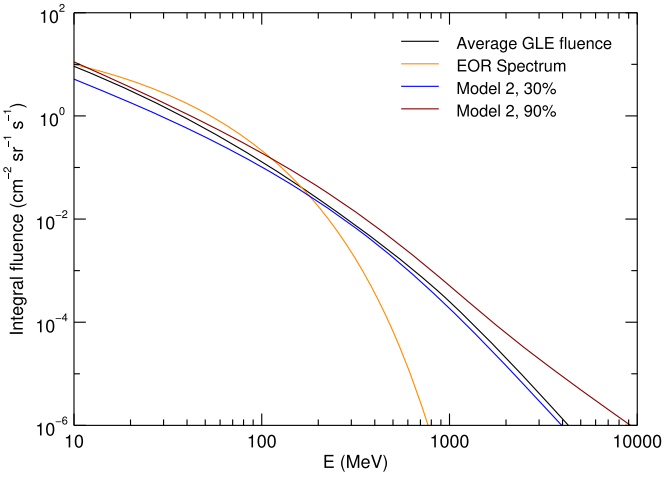

Fig. 15. Total GLE fluence averaged over the years 1956–2012 (in black), exponent-over-rigidity solar proton fluence spectrum averaged over 1954–2008 (Reedy, 2012, in orange), compared with spectra at 30% confidence (in blue) and 90% confidence (in red) simulated with model 2 for a mission of 37 years during solar active time and 20 years during solar quiet time.

solar proton models (JPL, ESP and SEPEM), despite the large differences in both the data and the methodologies used in the models. It is interesting to note the agreement at the lowest energies (below few tens of MeV), since the data used to construct the other models also includes non-GLE events, which may contribute with very large fluences at low energies. The agreement suggests that during the solar cycles 19–24, on average, GLEs have been responsible for a major portion of fluence even at low energies. On shorter timescales this is not necessarily the case; for example, during the first eight years of cycle 24 the total proton fluence at >10 MeV from sub-GLEs, calculated with the Band-fits (parameters given in Vainio et al., 2017), was about $7.9 \cdot 10^8\,\mathrm{cm}^{-2}\mathrm{sr}^{-1}$, whereas the only GLE of the period produced a fluence of about $6.6 \cdot 10^6\,\mathrm{cm}^{-2}\mathrm{sr}^{-1}$, i.e., two orders of magnitude smaller.

Our models benefit from the very long data aqcuisition period (over 5 complete solar cycles) as well as the extremely wide energy range (from 10 MeV to ~10 GeV). One limiting factor in the accuracy of our results is the small number of GLE episodes, $n_{GLE} = 49$, considered in our data. This number means that every result for probabilities smaller than $1/49 \approx 2.0\%$ comes purely from extrapolation. The statistics for high-fluence events could potentially be increased by studying historical cosmogenic isotope data (e.g., Usoskin et al., 2006; Miyake et al., 2012; Usoskin and Kovaltsov, 2012), but as was pointed out by Kovaltsov et al. (2014), this method depends strongly on the assumed spectral shape of events for integral fluences at energies lower or higher than >200 MeV. The occurrence rate of events used in our data is also very low (close to one event per year), and therefore modeling of missions with durations shorter than one year does not produce meaningful results.

Another factor that should be noted is the quality of satellite data used in the Band fitting. Recently, Sandberg et al. (2014) developed a method for cross-calibrating the medium energy GOES/EPS channels with corresponding channels of the science-level IMP-8/GME instrument. The effect of this cross-correlation was validated by Rodriguez et al. (2017) using STEREO observations (Mewaldt et al., 2008; von Rosenvinge et al., 2008). Sandberg et al. (2014) also noted some problems with the low energy IMP-8 data, attributed to the gradual failing of the LED instrument between 1984 and 1990. In addition, Smart and Shea (1999) described an intercalibration method for correcting side-penetration related discrepancies in the high energy spectrum measured by the GOES/HEPAD instrument; more recent work on GOES/HEPAD channels is being performed by Rodriguez (personal communication, 2016). These corrections for instrumental effects have not been performed on the data products which we used for the Band fitting.

Acknowledgements. The research described in this paper was partly supported by ESA Contracts 4000106133/12/NL/AF and 4000113187/15/D/MRP. We gratefully acknowledge the use of Hα and X-ray data made available at the NOAA STP

online service. We also acknowledge the important work of the PIs of the Neutron Monitors contributing their data to the world data centres. O.R. wishes to thank the Vilho, Yrjö and Kalle Väisälä foundation for financial support. We would also like to thank the two anonymous referees, whose comments helped to greatly improve the manuscript.

The editor thanks Ilya Usoskin and an anonymous referee for their assistance in evaluating this paper.

References

Asvestari E, Willamo T, Gil A, Usoskin IG, Kovaltsov GA, Mikhailov VV, Mayorov A. 2017. Analysis of ground level enhancements (GLE): extreme solar energetic particle events have hard spectra. *Adv Space Res* **60**: 781–787. DOI:10.1016/j.asr.2016.08.043.

Atwell W, Tylka AJ, Dietrich WF, Rojdev K, Matzkind C. Probability estimates of solar proton doses during periods of low sunspot number for short duration missions. In: Proceedings of the 46th International Conference on Environmental Systems. Vienna, Austria, 2016. URL: https://ttu-ir.tdl.org/ttu-ir/handle/2346/67739.

Baker DN, Mason GM, Figueroa O, Colon G, Watzin JG, Aleman RM. 1993. An overview of the Solar, Anomalous, and Magnetospheric Particle Explorer (SAMPEX) mission. *IEEE Trans Geosci Remote Sens* **31**: 531–541. DOI:10.1109/36.225519.

Band D, Matteson J, Ford L, Schaefer B, Palmer D et al. 1993. BATSE observations of gamma-ray burst spectra. I - Spectral diversity. *Astrophys J* **413**: 281–292. DOI:10.1086/172995.

Belov AV, Eroshenko EA, Kryakunova ON, Kurt VG, Yanke VG. 2010. Ground level enhancements of solar cosmic rays during the last three solar cycles. *Geomagn Aeron* **50**: 21–33. DOI:10.1134/S0016793210010032.

Clem JM, Dorman LI. 2000. Neutron monitor response functions. *Space Sci Rev* **93**: 335–359. DOI:10.1023/A:1026508915269.

Cliver EW. 2006. The unusual relativistic solar proton events of 1979 August 21 and 1981 May 10. *Astrophys J* **639**: 1206–1217. DOI:10.1086/499765.

Cliver EW, Kahler SW, Shea MA, Smart DF. 1982. Injection onsets of 2 GeV protons, 1 MeV electrons, and 100 KeV electrons in solar cosmic ray flares. *Astrophys J* **260**: 362–370. DOI:10.1086/160261.

Cohen CMS, Mewaldt RA, Leske RA, Cummings AC, Stone EC, Wiedenbeck ME, Christian ER, von Rosenvinge TT. 1999. New observations of heavy-ion-rich solar particle events from ACE. *Geophys Res Lett* **26**: 2697–2700. DOI:10.1029/1999GL900560.

Dallal GE, Wilkinson L. 1986. An analytic approximation to the distribution of Lilliefors's test statistic for normality. *Am Stat* **40**: 294–296. DOI:10.1080/00031305.1986.10475419.

Desai MI, Mason GM, Dayeh MA, Ebert RW, Mccomas DJ, Li G, Cohen CMS, Mewaldt RA, Schwadron NA, Smith CW. 2016a. Spectral properties of large gradual solar energetic particle events. I. Fe, O, and Seed material. *Astrophys J* **816**: 68. DOI:10.3847/0004-637X/816/2/68,

Desai MI, Mason GM, Dayeh MA, Ebert RW, McComas DJ, Li G, Cohen CMS, Mewaldt RA, Schwadron NA, Smith CW. 2016b. Spectral properties of large gradual solar energetic particle events. II. Systematic Q/M dependence of heavy ion spectral breaks. *Astrophys J* **828**: 106. DOI:10.3847/0004-637X/828/2/106.

Dodson HW, Hedeman ER. 1969. Solar circumstances at the time of the Cosmic ray increase on January 28, 1967. *Sol Phys* **9**: 278–295. DOI:10.1007/BF02391649.

Facius R, Reitz G. 2007. Space weather impacts on space radiation protection. In: Space Weather-Physics and Effects. Springer, Berlin, Heidelberg, 289–352. URL: http://dx.doi.org/10.1007/978-3-540-34578-7_11.

Feynman J, Armstrong TP, Dao-Gibner L, Silverman S. 1990. New interplanetary proton fluence model. *J Spacecr Rockets* **27**: 403–410. DOI:10.2514/3.26157.

Feynman J, Gabriel S. 1996. High-energy charged particles in space at one astronomical unit. *IEEE Trans Nucl Sci* **43**: 344–352. DOI:10.1109/23.490754.

Feynman J, Spitale G, Wang J, Gabriel S. 1993. Interplanetary proton fluence model – JPL 1991. *J Geophys Res: Space Phys* **98**: 13. DOI:10.1029/92JA02670.

Firoz KA, Cho K-S, Hwang J, Phani Kumar DV, Lee JJ, Oh SY, Kaushik SC, Kudela K,Rybanský M, Dorman LI. 2010. Characteristics of ground-level enhancement-associated solar flares, coronal mass ejections, and solar energetic particles. *J Geophys Res: Space Phys* **115**: A09105. DOI:10.1029/2009JA015023.

Glover A, Hilgers A, Rosenqvist L, Bourdarie S. 2008. Interplanetary proton cumulated fluence model update. *Adv Space Res* **42**: 1564–1568. DOI:10.1016/j.asr.2007.08.023.

Gopalswamy N, Xie H, Akiyama S, Yashiro S, Usoskin IG, Davila JM. 2013. The first ground level enhancement event of solar cycle 24: direct observation of shock formation and particle release heights. *Astrophys J Lett* **765**: L30. DOI:10.1088/2041-8205/765/2/L30.

Gopalswamy N, Xie H, Yashiro S, Akiyama S, Mäkelä P, Usoskin IG. 2012. Properties of ground level enhancement events and the associated solar eruptions during solar cycle 23. *Space Sci Rev* **171**: 23–60. DOI:10.1007/s11214-012-9890-4.

Grechnev VV, Kurt VG, Chertok IM, Uralov AM, Nakajima H et al. 2008. An extreme solar event of 20 January 2005: properties of the flare and the origin of energetic particles. *Sol Phys* **252**: 149–177. DOI:10.1007/s11207-008-9245-1.

Jiggens PTA, Gabriel SB, Heynderickx D, Crosby N, Glover A, Hilgers A. 2012. ESA SEPEM project: peak flux and fluence model. *IEEE Trans Nucl Sci* **59**: 1066–1077. DOI:10.1109/TNS.2012.2198242.

King JH. 1974. Solar proton fluences for 1977–1983 space missions. *J Spacecr Rocket* **11**: 401. DOI:10.2514/3.62088.

Kovaltsov GA, Usoskin IG, Cliver EW, Dietrich WF, Tylka AJ. 2014. Fluence ordering of solar energetic proton events using cosmogenic radionuclide data. *Sol Phys* **289**: 4691–4700. DOI:10.1007/s11207-014-0606-7.

Kudela K, Shea MA, Smart DF, Gentile LC. 1993. Relativistic solar particle events recorded by the Lomnicky Stit neutron monitor. In Leahy DA, Hicks RB, Venkatesan D, eds. Proceedings of the 23rd International Cosmic Ray Conference, 3, p. 71. Calgary, Canada. URL: http://adsabs.harvard.edu/abs/1993ICRC..3..71K.

Lanzerotti LJ. 2007. Space weather effects on communications. In: Space Weather-Physics and Effects. Springer, Praxis Publishing, Chichester, pp. 247–268. URL: http://dx.doi.org/10.1007/978-3-540-34578-7_9.

Lilliefors HA. 1967. On the Kolmogorov-Smirnov test for normality with mean and variance unknown. *J Am Stat Assoc* **62**: 399–402, URL: http://www.jstor.org/stable/2283970.

Mason GM, Mazur JE, Dwyer JR. 1999. ^{3}He enhancements in large solar energetic particle events. *Astrophys J Lett* **525**: L133–L136. DOI:10.1086/312349.

McCracken KG, Moraal H, Stoker PH. 2008. Investigation of the multiple-component structure of the 20 January 2005 cosmic ray ground level enhancement. *J Geophys Res: Space Phys* **113**: A12101, DOI:10.1029/2007JA012829.

McGuire RE, von Rosenvinge TT, McDonald FB. 1986. The composition of solar energetic particles. *Astrophys J* **301**: 938–961. DOI:10.1086/163958.

Mewaldt RA, Cohen CMS, Cook WR, Cummings AC, Davis AJ et al. 2008. The low-energy telescope (LET) and SEP central electronics for the STEREO mission. *Space Sci Rev* **136**: 285–362. DOI:10.1007/s11214-007-9288-x.

Mewaldt RA, Looper MD, Cohen CMS, Haggerty DK, Labrador AW, Leske RA, Mason GM, Mazur JE, von Rosenvinge TT. 2012. Energy spectra, composition, and other properties of ground-level events during solar cycle 23. *Space Sci Rev* **171**: 97–120. DOI:10.1007/s11214-012-9884-2.

Meyer J-P. 1985. The baseline composition of solar energetic particles. *Astrophys J Suppl Ser* **57**: 151–171. DOI:10.1086/191000.

Miyake F, Nagaya K, Masuda K, Nakamura T. 2012. A signature of cosmic-ray increase in AD 774-775 from tree rings in Japan. *Nature* **486**: 240–242. DOI:10.1038/nature11123.

Möbius E, Popecki M, Klecker B, Kistler LM, Bogdanov A et al. 1999. Energy dependence of the ionic charge state distribution during the November 1997 solar energetic particle event. *Geophys Res Lett* **26**: 145–148. DOI:10.1029/1998GL900131.

Nymmik RA. 1998. Radiation environment induced by cosmic ray particle fluxes in the international space station orbit according to recent galactic and solar cosmic ray models. *Adv Space Res* **21**: 1689–1698. DOI:10.1016/S0273-1177(98)00015-5.

Nymmik RA. 1999. Probabilistic model for fluences and peak fluxes of solar energetic particles. *Radiat Meas* **30**: 287–296. DOI:10.1016/S1350-4487(99)00065-7.

Nymmik RA, Panasyuk MI, Pervaja TI, Suslov AA. 1992. A model of galactic cosmic ray fluxes. *Nucl Tracks Radiat Meas* **20**: 427–429. DOI:10.1016/1359-0189(92)90028-T.

Onsager T, Grubb R, Kunches J, Matheson L, Speich D, Zwickl R, Sauer H. 1996. Operational uses of the GOES energetic particle detectors. Proceedings of SPIE, Denver, Colorado, USA, pp.281–290. DOI:10.1117/12.254075.

Reames DV. 1988. Bimodal abundances in the energetic particles of solar and interplanetary origin. *Astrophys J* **330**: L71–L75. DOI:10.1086/185207.

Reames DV. 1999. Particle acceleration at the Sun and in the heliosphere. *Space Sci Rev* **90**: 413–449. DOI:10.1023/A:1005105831781.

Reames DV. 2013. The two sources of solar energetic particles. *Space Sci Rev* **175**: 53–92. DOI:10.1007/s11214-013-9958-9.

Reames DV, von Rosenvinge TT, Lin RP. 1985. Solar He-3-rich events and nonrelativistic electron events – A new association. *Astrophys J* **292**: 716–724. DOI:10.1086/163203.

Reedy RC. 2012. Update on solar-proton fluxes during the last five solar activity cycles. In: 43rd Lunar and Planetary Science Conference, 1285. The Woodlands: Texas, USA, URL: http://adsabs.harvard.edu/abs/2012LPI..43.1285R.

Rodriguez JV, Sandberg I, Mewaldt RA, Daglis IA, Jiggens P. 2017. Validation of the effect of cross-calibrated GOES solar proton effective energies on derived integral fluxes by comparison with STEREO observations. *Space Weather* **15**: 290–309. DOI:10.1002/2016SW001533.

Rosenqvist L, Hilgers A, Evans H, Daly E, Hapgood M, Stamper R, Zwickl R, Bourdarie S, Boscher D. 2005. Toolkit for updating interplanetary proton cumulated fluence models. *J Spacecr Rocket* **42**: 1077–1090. DOI:10.2514/1.8211.

Sandberg I, Jiggens P, Heynderickx D, Daglis IA. 2014. Cross calibration of NOAA GOES solar proton detectors using corrected NASA IMP-8/GME data. *Geophys Res Lett* **41**: 4435–4441. DOI:10.1002/2014GL060469.

Sandroos A, Vainio R. 2007. Simulation results for heavy ion spectral variability in large gradual solar energetic particle events. *Astrophys J Lett* **662**: L127–L130. DOI:10.1086/519378.

Sandroos A, Vainio R. 2009. Reacceleration of flare ions in coronal and interplanetary shock waves. *Astrophys J Suppl Ser* **181**: 183–196. DOI:10.1088/0067-0049/181/1/183.

Shea MA, Smart DF. 2000. Fifty years of cosmic radiation data. *Space Sci Rev* **93**: 229–262. DOI:10.1023/A:1026500713452.

Shea MA, Smart DF, Gentile L, Campbell JM. 1995. Review of ground-level solar cosmic ray enhancements during the 22nd solar cycle. In N. Iucci, E. Lamanna, eds, Proceedings of the 24th International Cosmic Ray Conference, Rome, Italy, vol. 4, p. 244, URL: http://adsabs.harvard.edu/abs/1995ICRC..4.244S.

Simpson JA. 1958. Cosmic-radiation neutron intensity monitor. In: Annals of the Int. Geophysical Year IV, Part VII, 351, Pergamon Press, London. URL:http://nsidc.org/arc/archives-catalog/index.php?p=digitallibrary/getfileid=98.

Simpson JA, Fonger W, Treiman SB. 1953. Cosmic radiation intensity-time variations and their origin. I. Neutron intensity variation method and meteorological factors. *Phys Rev* **90**: 934–950. DOI:10.1103/PhysRev.90.934.

Singh AK, Siingh D, Singh RP. 2010. Space weather: physics, effects and predictability. *Surv Geophys* **31**: 581–638. DOI:10.1007/s10712-010-9103-1.

Smart DF, Shea MA. 1999. Comment on the use of GOES solar proton data and spectra in solar proton dose calculations. *Radiat Meas* **30**: 327–335. DOI:10.1016/S1350-4487(99)00059-1.

Smart DF, Shea MA, Tylka AJ, Boberg PR. 2006. A geomagnetic cutoff rigidity interpolation tool: accuracy verification and application to space weather. *Adv Space Res* **37**: 1206–1217, DOI:10.1016/j.asr.2006.02.011.

Stoker PH, Dorman LI, Clem JM. 2000. Neutron monitor design improvements. *Space Sci Rev* **93**: 361–380, DOI:10.1023/A:1026560932107.

Švestka Z, Simon P, eds. 1975. Catalog of solar particle events 1955-1969. *Astrophys Space Sci Libr* **49**: DOI:10.1007/978-94-010-1742-8.

Taylor B, Vacanti G, Maddox E, Underwood CI. 2011. The Interplanetary electron model (IEM). *IEEE Trans Nucl Sci* **58**: 2785–2792. DOI:10.1109/TNS.2011.2171718.

Thakur N, Gopalswamy N, Xie H, Mäkelä P, Yashiro S, Akiyama S, Davila JM. 2014. Ground level enhancement in the 2014 January 6 solar energetic particle event. *Astrophys J Lett* **790**: L13. DOI:10.1088/2041-8205/790/1/L13.

Tylka AJ, Cohen CMS, Dietrich WF, Lee MA, Maclennan CG, Mewaldt RA, Ng CK, Reames DV. 2005. Shock geometry, seed populations, and the origin of variable elemental composition at high energies in large gradual solar particle events. *Astrophys J* **625**: 474–495. DOI:10.1086/429384.

Tylka AJ, Dietrich WF. 2009. A new and comprehensive analysis of proton spectra in ground-level enhanced (gle) solar particle events. In: Proceedings of the 31st International Cosmic Ray Conference. M. Giller, J. Szabelski, eds, Poland. URL:http://icrc2009.uni.lodz.pl/proc/pdf/icrc0273.pdf.

Tylka AJ, Lee MA. 2006. A model for spectral and compositional variability at high energies in large, gradual solar particle events. *Astrophys J* **646**: 1319–1334. DOI:10.1086/505106.

Usoskin IG, Kovaltsov GA. 2012. Occurrence of extreme solar particle events: assessment from historical proxy data. *Astrophys J* **757**: 92. DOI:10.1088/0004-637X/757/1/92.

Usoskin IG, Solanki SK, Kovaltsov GA, Beer J, Kromer B. 2006. Solar proton events in cosmogenic isotope data. *Geophys Res Lett* **33**: L08107. DOI:10.1029/2006GL026059.

Vainio R, Desorgher L, Heynderickx D, Storini M, Flückiger E et al. 2009. Dynamics of the earth′s particle radiation environment. *Space Sci Rev* **147**: 187–231. DOI:10.1007/s11214-009-9496-7.

Vainio R, Raukunen O, Tylka AJ, Dietrich WF, Afanasiev A. 2017. Why is solar cycle 24 an inefficient producer of high-energy particle events? *Astron Astrophys* **604**: A47. DOI:10.1051/0004-6361/201730547.

von Rosenvinge TT, Reames DV, Baker R, Hawk J, Nolan JT et al. 2008. The high energy telescope for STEREO. *Space Sci Rev* **136**: 391–435. DOI:10.1007/s11214-007-9300-5.

Xapsos MA, O'Neill PM, O'Brien TP. 2013. Near-earth space radiation models. *IEEE Trans Nucl Sci* **60**: 1691–1705. DOI:10.1109/TNS.2012.2225846.

Xapsos MA, Stauffer C, Gee GB, Barth JL, Stassinopoulos EG, McGuire RE. 2004. Model for solar proton risk assessment. *IEEE Trans Nucl Sci* **51**: 3394–3398. DOI:10.1109/TNS.2004.839159.

Xapsos MA, Stauffer C, Jordan T, Barth JL, Mewaldt RA. 2007. Model for cumulative solar heavy ion energy and linear energy transfer spectra. *IEEE Trans Nucl Sci* **54**: 1985–1989. DOI:10.1109/TNS.2007.910850.

Xapsos MA, Summers GP, Barth JL, Stassinopoulos EG, Burke EA. 2000. Probability model for cumulative solar proton event fluences. *IEEE Trans Nucl Sci* **47**: 486–490. DOI:10.1109/23.856469.

Cite this article as: Raukunen O, Vainio R, Tylka AJ, Dietrich WF, Jiggens P, Heynderickx D, Dierckxsens M, Crosby N, Ganse U, Siipola R. 2018. Two solar proton fluence models based on ground level enhancement observations. *J. Space Weather Space Clim.* **8**: A04.